The Kelch13 compartment is a hub of highly divergent vesicle trafficking proteins in malaria parasites

Sabine Schmidt[1,§], Jan Stephan Wichers-Misterek[1,§], Hannah Michaela Behrens[1], Jakob Birnbaum[1], Isabelle Henshall[1], Ernst Jonscher[1], Sven Flemming[1], Carolina Castro-Peña[1], Tobias Spielmann[1,#]

[1] Bernhard Nocht Institute for Tropical Medicine, 20359 Hamburg, Germany

§ contributed equally, order determined alphabetically

Corresponding author: spielmann@bnitm.de

ORCID:

Sabine Schmidt:	0000-0002-6958-9832
Jan Stephan Wichers-Misterek:	0000-0002-0599-1742
Hannah Michaela Behrens:	0000-0002-7406-7086
Jakob Birnbaum:	0000-0002-1419-522X
Isabelle Henshall:	0000-0002-5906-0687
Ernst Jonscher:	0000-0002-8480-6102
Carolina Castro-Peña:	0000-0002-6878-4951
Tobias Spielmann:	0000-0002-3968-4601

ABSTRACT

Single amino acid changes in the parasite protein Kelch13 (K13) result in reduced susceptibility of *P. falciparum* parasites to Artemisinin and its derivatives (ART). Recent work indicated that K13 and other proteins co-localising with K13 (K13 compartment proteins) are involved in the endocytic uptake of host cell cytosol (HCCU) and that a reduction in HCCU results in ART resistance. HCCU is critical for parasite survival but is poorly understood, with the K13 compartment proteins among the few proteins so far functionally linked to this process. Here we further defined the composition of the K13 compartment by identifying four novel proteins at this site. Functional analyses, tests for ART susceptibility as well as comparisons of structural similarities using AlphaFold2 predictions of these and previously identified proteins showed that canonical vesicle trafficking and endocytosis domains were frequent in proteins involved in resistance and endocytosis, strengthening the link to endocytosis. Despite this, most showed unusual domain combinations and large parasite-specific regions, indicating a high level of taxon-specific adaptation. A second group of proteins did not influence endocytosis or ART susceptibility and was characterised by a lack of vesicle trafficking domains. We here identified the first essential protein of this second group and showed that it is needed in late-stage parasites. Overall, this work identified novel proteins functioning in endocytosis and at the K13 compartment. Together with comparisons of structural predictions it provides a repertoire of functional domains at the K13 compartment that indicate a high level of adaption of endocytosis in malaria parasites.

INTRODUCTION

Malaria is one of the deadliest infectious diseases, responsible for an estimated 627 000 deaths and 241 million cases in 2020 [1]. Malaria deaths have been declining in the last two decades [1,2]. One of the factors contributing to this reduction is efficient treatment which currently relies on artemisinin and its derivatives (ART) administered together with a partner drug [3]. However, parasites with a reduced susceptibility to ART have become widespread in South East Asia and now also emerged in Africa [4,5,14–16,6–13]. The reduced effectivity of ART was linked to a delayed parasite clearance in patients that is due to a decreased susceptibility of ring-stage parasites to ART [17,18], leading to recrudescence and treatment failure in patients [19–22]. Decreased susceptibility of ring-stage parasites can be measured *in vitro* using the ring stage survival assay (RSA) [23]. We here refer to this *in vitro* measurable phenomenon as "*in vitro* ART resistance" when the survival of parasites is above 1% in an RSA as previously defined [23]. Point mutations in the gene encoding the parasite protein Kelch13 (K13) are the main cause for the reduced ART susceptibility

of laboratory and field parasite isolates [24,25] and was shown to lead to decreased K13 protein levels [26–30]. This results in reduced hemoglobin uptake via endocytosis, which is assumed to cause less ART activation through hemoglobin degradation products, resulting in the reduced parasite ART susceptibility [26,31].

Endocytosis is a critical process for blood stage growth of malaria parasites. During its asexual development in erythrocytes the parasite uses this process to take up more than two-thirds of the soluble host cell content, which consists almost exclusively of hemoglobin [32–34]. The endocytosed host cell cytosol is transported to the acidic lysosome-like food vacuole (FV), where digestion of hemoglobin results in generation of free heme, which is further converted into nontoxic hemozoin [35,36]. Host cell cytosol uptake (HCCU) provides both space and building blocks (amino acids from digested hemoglobin) for parasite growth [33]. As a consequence, ART resistant parasites are hypersensitive to amino acid restriction, highlighting the importance of endocytosis for parasite growth and its connection to ART resistance [37,38]. Hemoglobin trafficking to the parasite food vacuole is believed to be initiated at membrane invaginations called cytostomes [27,33,39] followed by vesicular transport from the parasite plasma membrane (PPM) to the food vacuole [33,40], likely in an actin-myosin motor dependent manner [39,41–43]. The molecular effectors involved in this process remain poorly characterized and so far only VPS45 [44], the phosphoinositide-binding protein PX1 [45], the host enzyme peroxiredoxin 6 [46] and K13 and some of its compartment proteins (Eps15, AP2µ, KIC7, UBP1) [26] have been reported to act at different steps in the endocytic uptake pathway of hemoglobin. While inactivation of VPS45, PX1 or actin resulted in an accumulation of hemoglobin filled vesicles [43–45], indicative of a block during endosomal transport, no such vesicles were observed upon inactivation of K13 and its compartment proteins [26], suggesting a role of these proteins during initiation of endocytosis.

In previous work we used a quantitative BioID approach to identify proteins in close proximity to K13 and its interactor Eps15 [26]. We designated these proteins K13 interaction candidates (KICs) [26]. As the proteins identified by proximity labelling approaches not only include interactors but also proteins that are located in a close spatial position of the bait [47,48], we will here refer to the collective of these proteins as the "proxiome". We reasoned that due to the high rate of proteins that turned out to belong to the K13 compartment when validating the K13 BioID hits [26], the hit lists of these experiments might contain further proteins belonging to the K13 compartment. Here we identified and functionally analysed further candidates from the K13 proxiome and classify these and previously confirmed K13 compartment proteins. This revealed that the K13 compartment contains proteins suggestive of a highly divergent

endocytosis mechanism in malaria parasites but also a second group of proteins with other functions.

RESULTS

To identify novel K13 compartment proteins we further exploited previously described proximity-dependent biotinylation experiments that had used K13 or the K13 compartment protein Eps15 as bait, selecting enriched proteins not characterized in our previous work [26] (Table S1). In order to do this we excluded proteins that (i) had previously been analysed (ii) were either linked with or had been shown to localise to the inner membrane complex (IMC) (PF3D7_1345600 [49]; PF3D7_0109000 (PhIL1) [50–52]; PF3D7_0717600 (IMC32) [53]; PF3D7_0822900 (PIC2) [54], PF3D7_1018200 (PPP8) [54,55], (iii) are considered typical DiQ-BioID 'contaminants' (PF3D7_0708400 (HSP90) and PF3D7_1247400 (FKBP35) [26,56]), (iv) localised to the apical polar ring in *P. berghei* (PF3D7_1141300 (APR1) [57]), (v) localised to the nucleus PF3D7_1247400 (FKBP35) [58,59], (vi) were linked with the apicoplast (PF3D7_0721100 [60]) or (vi) were also present in BioID experiments using Clathrin heavy chain (CHC) as bait [26] (PF3D7_0408100). These selection criteria resulted in a candidate list of thirteen proteins (PF3D7_1438400 (MCA2), PF3D7_1243400, PF3D7_1365800, PF3D7_1447800, PF3D7_1142100, PF3D7_0103100 (VPS51), PF3D7_1329100 (MyoF), PF3D7_1329500, PF3D7_0405700 (UIS14), PF3D7_0907200, PF3D7_0204300, PF3D7_1117900 and PF3D7_1016200), of which the top ten were chosen as putative K13 compartment proteins for further characterization in this manuscript (Table 1, Table S1).

MCA2 is part of the K13 compartment and its truncation confers *in vitro* ART resistance

We previously identified metacaspase-2 (MCA2) as one of the top 5 most enriched proteins of the K13 BioID experiments, but endogenous C-terminal tagging with a 2xFKBP-GFP-2xFKBP tag was not achieved despite several attempts [26]. By screening of the MalariaGEN *Plasmodium falciparum* Community Project database [61] a SNP at amino acid position 1344 of MCA2 was identified that on its own leads to a stop codon, thereby removing the metacaspase (MCA) domain. According to MalariaGEN, this SNP is found in Africa with a mean prevalence of 52% and in South Asia with 5% prevalence [61]. As a previously generated truncation of MCA2 at amino acid position 57 ($MCA2^{TGD}$-GFP) rendered the parasites resistant to ART as judged by RSAs [26], we generated a second cell line with MCA2 disrupted at the Y1344 position ($MCA2^{Y1344Stop}$-GFP^{endo} parasites) (Figure 1A), to assess if this change could mediate resistance in the field. Subsequent analyses of African parasite isolates [62]

138 revealed that this change was always accompanied by a second change in the
139 following base, reverting the stop codon, indicating that this change is not of relevance
140 for resistance in endemic settings. However, as we had not so far been able to localise
141 MCA2, we took advantage of these parasites with the first 1344 amino acids of MCA2
142 fused to GFP to study its localisation. Correct integration of the construct into the *mca2*
143 genomic locus was confirmed by PCR (Figure S1A) and expression of the truncated
144 fusion protein was verified by Western blot (Figure S1A). Live cell imaging of
145 MCA2^{Y1344Stop}-GFP^{endo} parasites revealed expression of MCA2 throughout the
146 intraerythrocytic development cycle, appearing as a single focus in ring stage
147 parasites while two or more foci were detectable in trophozoites and schizonts (Figure
148 1B), in contrast to the predominantly cytosolic localisation of MCA2^{TGD}-GFP (Figure
149 S2A). As this localisation is reminiscent of K13 and KIC localisation [26,63] we
150 generated MCA2^{Y1344Stop}-GFP^{endo} parasite episomally co-expressing mCherry-K13
151 and spatial relationship of MCA2^{Y1344Stop}-GFP and K13 foci was quantified based on
152 fluorescence microscopy (Figure 1C). This analysis showed that 59% of the
153 MCA2^{Y1344Stop} foci overlapped with K13 foci, 20% of the foci showed partial overlap
154 and 21% of the MCA2^{Y1344Stop} foci did not overlap with K13 foci (Figure 1C), indicating
155 a presence of MCA2 at the K13 compartment. In order to exclude an effect of the
156 truncation on MCA2 localisation we generated parasites with an endogenously tagged
157 full length MCA2-3xHA using SLI [63] (Figure S1B) that episomally co-expressed
158 mCherry-K13 and performed immunofluorescence assays (IFA). These experiments
159 confirmed the focal localisation of MCA2. Quantification of the relative localisation of
160 MCA2 and K13 revealed that 44% of MCA2 foci overlapped with K13 (Figure S2B).
161 Partial overlap was observed for 24% of MCA2 foci, whereas 32% MCA2 foci did not
162 overlap with K13. Overall, these findings indicated that MCA2 is a K13 compartment
163 protein but is also found in additional, non-K13 compartment foci.
164
165 MCA2 was recently found to be enriched in BioID experiments with the inner
166 membrane complex (IMC) marker protein PhIL1 [54]. We generated MCA2^{Y1344Stop}-
167 GFP^{endo} parasites episomally co-expressing PhIL1mCherry and analysed schizont
168 stage parasites. Fluorescent imaging with these parasites revealed a close association
169 of MCA2^{Y1344Stop}-GFP foci with the IMC at the periphery of the newly formed
170 merozoites (Figure 1D), as previously observed for K13 [54]. Of note, no
171 MCA2^{Y1344Stop}-GFP foci were observed in free merozoites (Figure 1D). This data
172 indicates that MCA2 and the K13 compartment - as previously suggested [27,54] - are
173 found proximal to the IMC in schizonts.
174

We previously showed that a truncation of MCA2 at amino acid position 57 results in significantly reduced *in vitro* parasite proliferation [26]. Proliferation assays with the MCA2^{Y1344Stop}-GFP^{endo} parasites which express a larger portion of this protein yet still lack the MCA domain (Figure 1A) indicated no growth defect in these parasites compared to 3D7 wild type parasites (Figure 1E). Hence, the MCA domain in MCA2 does not appear to be needed for efficient *in vitro* blood stage growth.

Next, we performed a ring-stage survival assay (RSA) which revealed that the truncation of MCA2 at amino acid position Y1344 resulted in a reduced sensitivity to ART (Figure 1F). The mean parasite survival rate was 1.64%, which is above the defined ART resistance cut-off value of 1% [23], but lower than the ~5% survival rate of the MCA2-TGD parasites [26]. Overall, our results establish MCA2 as a member of the K13 compartment that has a function needed for optimal parasite growth during the intra-erythrocytic development cycle and that confers *in vitro* ART resistance when impaired. Its function facilitating for efficient parasite growth and, to a lesser extent, its influence on ART resistance were independent of its MCA domain.

MyosinF is involved in host cell cytosol uptake and associated with the K13 compartment

The identification of MyosinF (MyoF) in the K13 compartment DiQ-BioIDs could indicate an involvement of actin/myosin in endocytosis in malaria parasites as suspected based on actin inhibitor studies [41,43,64]. We therefore analysed its location in the cell. For this, we first generated transgenic parasites expressing a C-terminally 2xFKBP-GFP-2xFKBP tagged version expressed from its original locus using SLI (Figure S1C). Expression and localisation of the fusion protein was analysed by fluorescent microscopy. The tagged MyoF was detectable as foci close to the food vacuole from late ring stage / young trophozoite stage onwards, while in schizonts multiple MyoF foci were visible (Figure 2A). This expression pattern is in agreement with its transcriptional profile [65,66]. A similar localisation was observed in a cell line expressing MyoF with a smaller tag (MyoF-2xFKBP-GFP) from its endogenous locus (Figure S1D, Figure S3A). The proximity of the MyoF foci to the food vacuole was also evident by co-localisation with an episomally expressed food vacuole marker (P40PXmCherry) (Figure 2B). Next, we used the MyoF-2xFKBP-GFP-2xFKBP^{endo} parasites to generate a cell line episomally co-expressing mCherry-K13 (Figure 2C). Quantification from live fluorescence images revealed that 8% of MyoF foci overlapped with K13 foci, 12% showed a partial overlap, 36% were close together (touching but not overlapping), while 44% of MyoF foci were further away from K13 foci (Figure 2C). As the GFP-tagging of MyoF appeared to have some effect on the parasite (see

below), we validated the MyoF localisation by generating parasites with an endogenously 3xHA-tagged MyoF (MyoF-3xHA^{endo} parasites) using SLI (Figure S1E) and episomally co-expressed mCherry-K13. IFA confirmed the focal localisation of MyoF and its spatial association with mCherry-K13 foci (Figure S3B). We also detected MyoF signal in ring stage parasites (Figure S3B). As we did not detect the GFP-tagged version in rings, this might indicate low level expression of MyoF in ring stage parasites. Taken together these results show that MyoF is in foci that are frequently close or overlapping with K13, indicating that MyoF is found in a regular close spatial association with the K13 compartment and at times overlaps with that compartment.

During routine *in vitro* culturing we noticed that MyoF-2xFKBP-GFP-2xFKBP^{endo} parasites grew poorly and subsequent flow cytometry-based proliferation assays revealed a mean relative growth of 36.7% compared to 3D7 wild type parasites after two replication cycles (Figure 2D). These results indicated that C-terminal 2xFKBP-GFP-2xFKBP tagging of MyoF impaired its function and that this protein has an important role for the growth of asexual blood stages. We therefore generated MyoF-2xFKBP-GFP-2xFKBP^{endo} parasites episomally expressing a nuclear mislocaliser (1xNLS-FRB-mCherry) in order to conditionally inactivate it using knock-sideways. This system allows the conditional mislocalisation of a protein from its site of action into the nucleus upon addition of rapalog [63,67,68]. Assessment of mislocalisation efficacy by fluorescent microscopy at 1 hour post induction and 22 hours post induction revealed only partial mislocalisation of MyoF-2xFKBP-GFP-2xFKBP to the nucleus with some MyoF remaining at foci close to the food vacuole (Figure 2E). Despite the only partial inactivation of MyoF by knock sideways, flow cytometry-based proliferation assays revealed a 40.5% reduced parasitemia after two replication cycles upon addition of rapalog compared to control parasites without rapalog, while such an effect was not observed for 3D7 wild type parasites upon addition of rapalog (Figure 2F, Figure S3D). Hence, conditional inactivation of MyoF further reduced growth despite the fact that the tag on MyoF already led to a substantial growth defect.

Inspection of the MyoF-2xFKBP-GFP-2xFKBP^{endo}, compared to 3D7 wild type-trophozoites, revealed an increased number of vesicles in the parasite cytoplasm (Figure 2G), resembling the phenotype observed after inactivation of VPS45 [44]. This was even more pronounced upon inactivation of MyoF (Figure 2G), suggesting this is due to a reduced function of MyoF. Additionally, we directly tested for an effect of MyoF inactivation on HCCU using a ‘bloated food vacuole assay’ [44]. For this we incubated parasites upon MyoF inactivation (and control parasites without rapalog) with the protease inhibitor E64 [69]. In the presence of E64, newly internalized hemoglobin

cannot be degraded and accumulates in the food vacuole, resulting in bloated food vacuoles. While 88% of control parasites developed bloated food vacuoles, only 52% of the cells with inactivated MyoF showed a bloated food vacuole (Figure 2H, Figure S3E), indicating that less hemoglobin reached the food vacuole upon inactivation of MyoF.

Finally, we also tested if inactivation of MyoF has an effect on *in vitro* ART resistance. RSAs [23] revealed no significant increase in parasite survival upon MyoF inactivation with neither 12 h nor 24 h rapalog pre-incubation (Figure 2I, Figure S3F). Overall, our results indicate a close association of MyoF foci with the K13 compartment and a role of MyoF in endocytosis albeit at a different step than K13 compartment proteins.

KIC11 is a K13 compartment associated protein important for asexual parasite proliferation, but not involved in endocytosis or ART resistance

PF3D7_1142100, currently annotated as 'conserved Plasmodium protein, unknown function', was renamed K13 interacting candidate 11 (KIC11), following the previously established nomenclature for potential K13 compartment proteins [26]. In order to test whether KIC11 is a member of the K13 compartment or not, we first generated transgenic parasites expressing it as a C-terminally 2xFKBP-GFP-2xFKBP tagged fusion protein from the original genomic locus using SLI (KIC11-2xFKBP-GFP-2xFKBP^{endo} parasites). Correct genomic modification of the *kic11* locus was verified by PCR (Figure S1F). The tagged KIC11 was poorly detectable in rings (preventing a meaningful assessment of localisation) but showed several foci from the trophozoite stage onwards, while in schizonts many KIC11-2xFKBP-GFP-2xFKBP foci were visible (Figure 3A). Next, we generated KIC11-2xFKBP-GFP-2xFKBP^{endo} parasites episomally co-expressing mCherry-K13. Fluorescence microscopy showed overlap of the foci of both fusion proteins in trophozoites, while in schizonts only some foci overlapped (Figure 3B). We conclude that KIC11 is a protein located at the K13 compartment in trophozoites and to a lesser extent in schizonts.

In order to assess the importance of KIC11 for parasite proliferation, we generated KIC11-2xFKBP-GFP-2xFKBP^{endo} parasites episomally co-expressing the nuclear mislocaliser 1xNLS-FRB-mCherry, enabling conditional inactivation by knock-sideways. Addition of rapalog resulted in efficient mislocalisation of KIC11-2xFKBP-GFP-2xFKBP into the nucleus 4 and 16 hours post induction (Figure 3C). Assessment of parasite proliferation by flow-cytometry over two developmental cycles revealed a mean relative growth of 10.3% compared to control parasites, indicating an important function of KIC11 for asexual parasite proliferation (Figure 3D, Figure S4A). This

interpretation was supported by several unsuccessful attempts to generate a cell line with a truncated *kic11* using the SLI-TGD system [63].

To better characterize the growth phenotype of the KIC11 knock-sideways, we added rapalog to tightly synchronised parasites at different time points (4, 24, and 32 hpi) and monitored parasite growth by flow cytometry. Additionally, we quantified parasite stage in Giemsa smears at 6, 24, 32, 40, 48, 72, and 96 hpi. While no effect on parasitemia and stage distribution was observed during growth in the first cycle, a reduced number of newly formed ring stage parasites was obvious at 48 hpi for all three rapalog addition time points, indicating an effect on parasite viability in late schizont or merozoites but no other stage (Figure 3E-F, Figure S4B). As the trophozoites with inactivated KIC11 developed into schizonts without morphological differences to controls (Figure 3F), KIC11 does not appear to be needed for endocytosis. To directly address this we tested if inactivation of KIC11 influences *in vitro* ART resistance (based on RSA) or endocytosis (using bloated food vacuole assays), but no significant differences were observed (Figure 3G-I, Figure S4C,D). Overall, our results indicate that KIC11 is part of the K13 compartment in trophozoites and that it has an important role for asexual parasite proliferation in late-stage parasites, which is in contrast to previously characterised essential K13 compartment proteins. These findings indicate that there are also K13 compartment proteins that have an important function not related to endocytosis.

KIC12 is located in the nucleus and at the K13 compartment and is involved in endocytosis but not in ART resistance

PF3D7_1329500, currently annotated as ‘conserved protein, unknown function’ was renamed K13 interacting candidate 12 (KIC12). In order to test whether KIC12 is a member of the K13 compartment or not, we first generated transgenic parasites expressing C-terminally 2xFKBP-GFP-2xFKBP tagged KIC12 from its original genomic locus (KIC12-2xFKBP-GFP-2xFKBP^{endo} parasites) (Figure S1G). Expression and localisation of tagged KIC12 was analysed by fluorescent microscopy. KIC12 was detectable in the nucleus in ring stage parasites. In trophozoites foci in the parasite periphery (Figure 4A, white arrows) were observed in addition to the signal in the nucleus (Figure 4A, light blue arrows). In schizonts these foci were not present anymore. Instead, only the nuclear signal and a faint uniform cytoplasmic GFP signal was detected in early schizonts and these signals both disappeared in later schizonts (Figure 4A, Figure S5A). In line with this expression pattern, the *kic12* transcriptional profile indicate mRNA levels peaks in merozoites and early ring-stage parasites and no RNA expression in trophozoites and schizonts [65,66,70]. Next, we generated KIC12-2xFKBP-GFP-2xFKBP^{endo} parasites episomally co-expressing mCherry-K13

which revealed an overlap of the KIC12 foci in the cell periphery with the K13 foci in trophozoites (Figure 4B, Figure S5A). In rings, the K13 foci did not overlap with KIC12, in agreement with the exclusively nuclear localisation of KIC12 in that stage (Figure 4B). We conclude that KIC12 is a protein with a dual location in the nucleus and the K13 compartment in trophozoites.

In order to assess the importance of KIC12 for parasite proliferation, we generated KIC12-2xFKBP-GFP-2xFKBP^{endo} enabling conditional inactivation by knock-sideways using a nuclear (1xNLS-FRB-mCherry) mislocaliser. Efficient mislocalisation of KIC12-2xFKBP-GFP-2xFKBP into the nucleus and absence of KIC12 foci in the cytoplasm of trophozoites upon addition of rapalog was confirmed by microscopy at 4 and 16 hours post induction (Figure 4C). Assessing parasite proliferation after knock sideways of KIC12 showed a mean relative growth of 37.0% compared to control parasites after two development cycles, indicating an important function of KIC12 for asexual parasite proliferation (Figure 4D; Figure S5B). Due to the dual localisation of KIC12 we also generated KIC12-2xFKBP-GFP-2xFKBP^{endo} parasites episomally co-expressing an alternative mislocaliser (Lyn-FRB-mCherry) [63], enabling conditional inactivation of the nuclear pool of KIC12-2xFKBP-GFP-2xFKBP by mislocalisation to the parasite plasma membrane (PPM), an approach previously shown to be suitable for efficiently inactivate nuclear proteins [63,71]. Induction of KIC12 mislocalisation to the PPM resulted in a loss of KIC12 in the nucleus 4 hours post induction (Figure 4E). Foci were still detected in the parasite periphery and it is unclear whether these remained with the K13 compartment or were also in some way affected by the Lyn-mislocaliser. Parasite proliferation assays revealed a growth defect of 49.2%, compared with 37.0% of the nuclear mislocalisation approach (Figure 4D; Figure S5C). The small difference between the two mislocalisers and the unclear influence on PPM foci of the Lyn mislocaliser does not permit a clear interpretation in regard to the functional importance of KIC12 at the two locations (nucleus and K13 compartment) of KIC12. However, these data overall confirm that KIC12 is important for efficient growth of asexual blood stages. The importance of KIC12 for asexual parasite proliferation was further supported by failure to obtain a cell line with a truncated *kic12* using the SLI-TGD system.

Based on the presence at the K13 compartment in trophozoites, we tested the effect of KIC12 inactivation on endocytosis. Bloated food vacuole assays showed that >99% of control parasites developed bloated food vacuoles, while only 49,3% (NLS mislocaliser) or 72.9% (Lyn mislocaliser) of the cells with inactivated KIC12 showed a bloated food vacuole (Figure 4F, Figure S5D), indicating an effect on endocytosis of host cell cytosol. As the effect was only partial, we decided to measure the parasite

and food vacuole size. This analysis with the KIC12 NLS mislocaliser parasites revealed a significantly reduced food vacuole size in the parasites with inactivated KIC12, while there was no effect on parasite size (Figure 4G; Figure S5 E-F). Plotting the values of the individual parasites showed that the food vacuoles of similarly sized parasites were consistently smaller in the KIC12 knock sideways compared to controls (Figure 4H), indicating that the effect on hemoglobin delivery to the food vacuole upon inactivation of KIC12 was not an indirect effect due to parasite growth impairment during the assay time. Similar results were obtained using the KIC12 Lyn mislocaliser line (Figure 4I-J). Quantification of the number of vesicles in trophozoites upon inactivation (with either the NLS or Lyn mislocaliser) of KIC12 revealed no difference to control (Figure 4K), indicating that KIC12 acted early in endocytosis, similar to the previously studied K13 compartment proteins [26].

Finally, we also tested if inactivation of KIC12 by mislocalisation to the nucleus has an effect on *in vitro* ART resistance, but congruent with the lacking co-localisation of KIC12 with K13 in rings, RSAs showed no significantly decreased ART susceptibility (Figure 4L, Figure S5G). Overall, our results indicate the presence of KIC12 at the K13 compartment in trophozoites, a role in HCCU and an additional pool of KIC12 in the nucleus.

Candidate proteins not detected at the K13 compartment

We also generated parasites expressing endogenously C-terminally 2xFKBP-GFP-2xFKBP tagged UIS14, PF3D7_1365800, PF3D7_1447800, PF3D7_0907200 and VPS51 and episomally co-expressed mCherry-K13 (Figure S1H-L). Fluorescence microscopy revealed no clear association with the K13 compartment in rings and trophozoites in any of these parasite lines. Instead UIS14, PF3D7_1447800 and VPS51 showed GFP foci within the parasite cytosol without consistent overlap with mCherry-K13 foci (Figure S6A,D,F), PF3D7_0907200 showed a weak cytosolic GFP signal and PF3D7_1365800 showed cytosolic GFP signal with additional foci closely associated with the nucleus without consistent overlap of the main foci with mCherry-K13 foci (Figure S6G and Figure S7A-B). Several attempts to generate PF3D7_1243400-2xFKBP-GFP-2xFKBP^{endo} parasites remained unsuccessful, indicating the gene might be refractory to C-terminal modification and hence might be essential. For *vps51* and *uis14* we additionally were able to generate targeted gene disruption cell lines (Figure S1M-N, Figure S6B,E), indicating these candidates are dispensability for *in vitro* asexual parasite proliferation, although growth assays indicated a need of UIS14 for optimal growth (Figure S6C).

Structural homology search [72] revealed the presence of a N-terminal arfaptin homology (AH) domain in PF3D7_1365800 (Figure S8C), a domain known to promote binding of arfaptin to Arf and Rho family GTPases important for vesicle budding at the Golgi [73,74]. Given that in *Toxoplasma* an intersection of endocytosis and secretion was observed at the trans Golgi [75], we tested the potential (indirect) influence of this protein on endocytosis related processes. We performed conditional inactivation using knock-sideways, but despite efficient loss of the PF3D7_1365800 foci no growth defect was observed (Figure S7C-D) and co-expression of the Golgi marker GRASP [76] revealed no consistent overlap between the foci of these two proteins (Figure S7E).

Based on this analysis we did not classify UIS14, PF3D7_1365800, PF3D7_1447800, PF3D7_0907200, and VPS51 as K13 compartment proteins and the location of PF3D7_1243400 remains unknown.

The domain repertoire in K13-compartment proteins

With the extended complement of K13 compartment proteins from this and previous work [26], we assessed the repertoire of functional domains at this site. For this we took advantage of recent advances in protein structure prediction to identify structural similarities in K13-compartment members for which no information could be inferred from sequence homology. We compared their structures predicted with the AlphaFold algorithm [72,77] with experimentally determined protein structures in the Protein Data Bank and identified 25 domains, 15 of which were not previously identified according to PlasmoDB and Interpro (Figure 5A,B and S8).

The largest number of recognisable folds were detected in KIC4, a protein for which we previously detected some similarity to α-adaptins [26]. KIC4 contained an N-terminal VHS domain (IPR002014), followed by a GAT domain (IPR004152) and an Ig-like clathrin adaptor α/β/γ adaptin appendage domain (IPR008152) (Figure 5A-C, Figure S8). This is an arrangement typical for GGAs (Golgi-localised gamma ear-containing Arf-binding proteins) which are vesicle adaptors first found to function at the trans-Golgi [78,79]. Surprisingly, KIC4 however also contains an additional domain at its C-terminus, a β-adaptin appendage C-terminal subdomain (IPR015151) which is a part of the ear domain of β-adaptins and not found in GGAs. Together with the preceding clathrin adaptor α/β/γ adaptin domain, the C-terminus of KIC4 therefore resembles a β-adaptin. The region without detectable fold after the GAT domain likely corresponds to the hinge region in GGAs. This suggests that KIC4 is a hybrid between GGAs and an AP complex subunit beta (Figure 5C), the two known types of adaptors.

Based on Interpro [80], such a domain organization has to date not been observed in any other protein.

KIC5 also contains a clathrin adaptor α/β/γ-adaptin domain (IPR008152) and one of the two subdomains of the ear domain of α-adaptins (clathrin adaptor α-adaptin_appendage C-terminal subdomain, IPR003164) (Figure 5 A,B,D). More than 97% of proteins containing these domains also contain an Adaptin_N (IPR002553) domain and function in vesicle adaptor complexes as subunit α (Figure 5D) but no such domain was detectable in KIC5. KIC5 thus displays some similarities to AP complex subunit α but similar to KIC4, there appear to be profound difference to the canonical adaptors.

KIC7 contains an ArfGAP domain, as recently also predicted for its *Toxoplasma* homolog AGFG (TGME49_257070) [81]. ArfGAPs regulate the activity of Arfs which are small GTP binding proteins coordinating vesicle trafficking [82,83]. UBP1 contains a ubiquitin specific protease (USP) domain at its C-terminus which previously led to its name ubiquitin carboxyl-terminal hydrolase 1 (UBP1) [84]. Here we also identified a VHS domain in its centre. VHS domains occur in vesicular trafficking proteins, particularly in endocytosis proteins, but typically are found at the N-terminus of proteins (in over 99.8% of cases according to annotations by Interpro). A combination with a USP domain has not been observed so far. If the VHS domain is functional in UBP1 despite its central position, it is the first structural domain that would support the functional data [26] showing this K13 compartment protein has a role in endocytosis.

In KIC12 we identified a potential purple acid phosphatase (PAP) domain. However, with the high RMSD of 4.9 Å, the domain might also be a divergent similar fold, such as a C2 domain, which targets proteins to membranes. KIC2 contains a GAR domain which typically bind the cytoskeleton [85] and KIC3 contains a PAH domain which can serve as a scaffold for transcription factors [86,87]. While not consistently detected at the K13 compartment, it is interesting that we here found that PF3D7_1365800 contains an AH domain, a member of the AH/BAR domain family (Figure S8C). According to Interpro, no AH or BAR domain proteins have so far been detected in malaria parasites, rendering this an interesting protein. However, as we here found it to be likely dispensable for intra-erythrocytic parasite development and in light of no strong indication for the presence in regions containing K13, it seems to be of little relevance for endocytosis.

Overall this analysis revealed that most of the proteins involved in endocytosis or *in vitro* ART resistance contain regions with structural homology to vesicle trafficking

domains, often specific for endocytosis (Figure 6E). However, apart from AP2 the domain arrangements are unusual, the conservation on the primary sequence level is low (which precluded initial detection) and there are large regions without any resemblance to other proteins, altogether indicating strong parasite-specific adaptations. In contrast, the K13 compartment proteins where no role in ART resistance (based on RSA) or endocytosis was detected, such as KIC2 or KIC11, do not contain such domains (Figure 6E). This analysis suggests that proteins detected at the K13 compartment can be classified into at least two groups of which one is involved in endocytosis and *in vitro* ART resistance whereas the other might have different functions yet to be discovered.

DISCUSSION

The BioID proxiome of K13 and Eps15 revealed the first proteins involved in the initial steps of endocytosis in malaria parasites, a process that in blood stage parasites leads to the uptake of large quantities of host cell cytosol. As demonstrated in model organisms, endocytosis is a complex and highly regulated process involving a multitude of proteins [88–90], but in Apicomplexan parasites is not well studied [33]. Thus, the K13 compartment proxiome represents an opportunity to identify proteins involved in this process in malaria parasites and will be important to understand it on a mechanistic level. Understanding how and if HCCU differs from the canonical endocytic processes in human cells, will not only help to understand this critical process in parasite biology but might also reveal parasite-specific aspects that permit specific inhibition and could be targets for drug development efforts.

Here we expanded the repertoire of K13 compartment proteins and functionally analysed several of them. An assessment of structural similarities indicated an abundance of vesicle trafficking - and more specifically - endocytosis domains, in the confirmed K13 compartment proteins. The proteins with such domains now comprise KIC4, KIC5, KIC7, Eps15, AP2µ and UBP1, all of which reduce *in vitro* ART susceptibility when inactivated, indicating that this led to a reduced endocytosis in ring stages [26]. A role in endocytosis has been experimentally shown for all of these except for KIC4 and KIC5, for which only gene disruptions are available which are less suitable for endocytosis assays [26].

Besides the AP2 complex, the structural similarity analysis indicated that two additional K13 compartment proteins (KIC4 and KIC5) contain domains found in adaptor subunits. KIC4 and KIC5 likely have additional rather than redundant roles to the AP2 complex, as the AP2 complex is essential for blood stage growth and on its own needed for HCCU [26,91]. While KIC4 disruption did not lead to a growth defect,

disruption of KIC5 impaired parasite growth [26], indicating that there cannot be full redundancy between these two proteins either. Altogether these considerations support specific individual roles of all the known K13 compartment proteins with adaptor domains.

In model organisms, the α/β/γ-adaptin appendage domain, the α-adaptin domain and the β-adaptin domain, in the AP2 complex and/or in GGAs, act as interaction hubs for more than 15 accessory proteins, including Eps15, Arfs, amphiphysin, epsins and rabaptins as well as lipids involved in vesicle budding [92]. This fits with the presence of Eps15 and KIC7 (which contains an ArfGAP domain) at the K13 compartment. The interaction between the α/β/γ-adaptin appendage domain and Eps15 has been captured by X-ray crystallography (2I9V) [92], highlighting a possible functional connection between Eps15 and AP-2α, AP-2β, KIC4 or KIC5, which all contain this domain. Indeed, the *Toxoplasma* homologue of KIC4 has recently been shown to bind Eps15, while *Tg*AP-2α did not [81].

Despite the detection of various domains in K13 compartment proteins it is noteworthy that most of these proteins (e.g. EPS15, UBP1, KIC7) still contain large regions without any homology to other proteins. The parasite-specific nature of the initial steps of endocytosis is also evident from the difficulty of primary sequence-based detection of the vesicular trafficking domains in K13 compartment proteins and from the unusual domain combinations. Furthermore it is peculiar that despite the presence of the clathrin adaptor AP2, clathrin itself does not seem to be involved [26,91], further indicating parasite-specific features of HCCU. Overall, this indicates a strongly adapted mechanism of the first steps in endocytosis for HCCU in malaria parasites. One protein typically involved in endocytosis that did not appear in the list of highly enriched proteins of the K13 and Eps15 proxiome is a dynamin [93] which might indicate further differences to the canonical mechanism in model organism. However, at least in *Toxoplasma* an association of K13 and its compartment with a dynamin was reported [81,94], indicating that an equivalent is likely also present in malaria parasites.

A protein that has a more canonical structure is MyoF, a Class XXII myosin [95], which we here link with endocytosis and found in foci that were often close or overlapping with the K13 compartment. The only partial overlap could indicate that either it i) only transiently associates with the K13 compartment, or ii) is in a separate compartment that is close to the K13 compartment or iii) is in a region of the K13 compartment that is close, but non-overlapping, with that defined by the other K13 compartment proteins. A number of conclusions can be drawn from our MyoF characterisation. Firstly, its

inactivation resulted in the appearance of vesicles, similar to the phenotype of VPS45 inactivation [44], indicating it has a role in endosomal transport, downstream of the initial steps of endocytosis. This is in contrast to the other K13 compartment proteins and might explain the only partial overlap in location of MyoF with the K13 compartment. Secondly, its involvement suggests a role of actin/myosin in endosomal transport which is well known from other organisms [96,97] and supports the observation that the actin inhibitor CytochalasinD leads to vesicles similar to MyoF inactivation [39,43]. Hence, myosin may generate force needed for the transport of host cell cytosol filled vesicles to the food vacuole. Thirdly, there was no effect of MyoF inactivation on ART resistance, which might indicate that there is no need for actin/myosin for endocytosis in rings. Although there were some limitations to our system to study MyoF, the substantial inactivation caused by simply tagging MyoF would already have led to a decreased susceptibility to ART in RSAs (as seen with other K13 compartment proteins [26]), if ring stage endocytosis had been affected, which was not the case. It is of note that the endocytosis function of MyoF is reciprocal to that of K13 which is only required in rings, indicating that there appear to be stage-specific differences in endocytosis between these stages. However, the majority of components are at the K13 compartment throughout the cycle and for instance KIC7 is needed for HCCU in both rings and trophozoites [26].

Attempts to generate a knockout of *P. berghei myof* were reported to be unsuccessful [95], while a genome-wide mutagenesis screen predicted *Pf*MyoF to be dispensable for asexual blood stage development [98]. *Tg*MyoF has been previously implicated in Golgi and rhoptry positioning [99] or centrosomes positioning and apicoplast inheritance [100]. We cannot exclude that beside the effect on HCCU, a part of the growth defect we see after MyoF inactivation arises from similar functions in blood stages.

MCA2 has been identified as putative K13 interaction candidate, but its location was unknown [26]. Here, we establish MCA2 as member of the K13 compartment by endogenously tagging it with HA as well as by using a cell line with a truncated MCA2 fused to GFP. MCA2 was located in foci overlapping with the K13 compartment and in schizonts the foci were in proximity of the IMC in line with previous data linking the K13 compartment and the IMC [54]. A close association of the K13 compartment and the IMC is also supported by recent work in *T. gondii* showing that the K13 compartment and its proteins are present at the IMC embedded micropore [81].

We previously showed that gene disruption of *mca2* results in reduced *in vitro* parasite proliferation and *in vitro* ART resistance [26], which is also supported by a knockout of

the *mca2* homologue in the rodent infecting *P. berghei* [101,102]. Truncation of MCA2 at amino acid position Y1344 still resulted in decreased ART susceptibility, even though the susceptibility reduction was less than a disruption at amino acid position 57. In contrast to the full disruption, truncation at residue 1344 did not lead to a growth defect, indicating that the predicted metacaspase domain (AA 1527-1848) – not present in this truncated MCA2 protein – is dispensable for asexual parasite proliferation. This finding is in contrast to results indicating an important role of the metacaspase domain for parasite proliferation using MCA2 inhibitors [103–105].

Here we also identified the first protein, KIC11, at the K13 compartment that had an important function for the growth of blood stage parasites but did not appear to function in endocytosis. Instead, KIC11 had an important function in late-stage parasites. KIC11 was predicted to be non-essential by a genome-wide mutagenesis screen [98], while the orthologue in the rodent malaria parasite *P. berghei* (PBANKA_0906900) was classified as essential for asexual proliferation in the PlasmoGem screen [106].

Overall the classification of K13 compartment proteins presented in this work indicates that there are two main groups. The first group comprises proteins that define a highly unusual endocytic pathway to internalise host cell cytosol. These proteins are predominately parasite-specific (exceptions being AP2µ, MyoF and in part K13 which however lacks vesicle trafficking domains). This group can be further categorised into a larger subgroup that is involved in *in vitro* ART resistance and a smaller subgroup, such as KIC12 and MyoF that do not confer *in vitro* ART resistance when inactivated, presumably because they are not needed for endocytosis in rings. In the case of MyoF this idea is supported by low expression in rings whereas KIC12 was not at the K13 compartment in rings. Reciprocal to this, we found in previous work that K13 is needed for endocytosis in ring stages only [26]. Hence, there is heterogeneity in the stage-specificity of the endocytosis proteins at the K13 compartment. In terms of function, most of the endocytosis and *in vitro* ART resistance group of K13 compartment proteins are involved in the initial phase of HCCU. In contrast to VPS45 [44] their inactivation does not result in the generation of endosomal intermediates in the parasite cytoplasm. The exception is MyoF which (of the proteins here classified as K13 compartment associated) generated vesicles when inactivated. MyoF showed the lowest spatial overlap with K13 and may form a link to downstream steps of endosomal transport. The second group of K13 compartment proteins has no role in endocytosis or *in vitro* ART resistance and do not contain vesicle trafficking domains (as based on our domain identification here). They likely serve other functions but the homogeneity of functions of this group is unclear. KIC11, the first essential protein of this group, might help to shed light on the function of the non-endocytosis related K13

compartment proteins. However, it should be noted that KIC11 showed only partial overlap with the K13 compartment in schizonts, the stage relevant for the observed phenotype of the inactivation of this protein. Hence, it is possible that KIC11's essential function is not at the K13 compartment. Overall, this work strengthens the notion that the K13 compartment is involved in endocytosis, reveals novel essential HCCU proteins and provides a classification of its members that might inform future studies to understand the unusual mechanism of endocytosis in apicomplexans.

METHODS

P. falciparum culture

Blood stages of *P. falciparum* 3D7 [107] were cultured in human red blood cells (O+ ; University Medical Center Hamburg, Eppendorf (UKE)). Cultures were maintained at 37°C in an atmosphere of 1 % O_2, 5 % CO_2 and 94 % N_2 using RPMI complete medium containing 0.5 % Albumax according to standard protocols [108].

In order to obtain highly synchronous parasite cultures, late schizonts were isolated by percoll gradient [109] and cultured with fresh erythrocytes for 4 hours. Afterwards sorbitol synchronization [110] was applied in order to remove remaining schizonts resulting in a highly synchronous ring stage parasite culture with a four-hour age window.

Cloning of plasmid constructs for parasite transfection

For endogenous C-terminal 2x-FKBP-GFP-2xFKBP tagging using the SLI system [63] a homology region of 321-1044 bp (1044 bp for *Pfmyof* (PF3D7_1329100), 690 bp for *Pfkic11* (PF3D7_1142100), 780 bp for PF3D7_1447800, 695 bp for *Pfkic12* (PF3D7_1329500), 411 bp for PF3D7_1243400, 321 bp for PF3D7_1365800, 674 bp for *Pfuis14* (PF3D7_0405700), 698 bp for PF3D7_0907200, 756 bp for *Pfvps51* (PF3D7_0103100)) was amplified from 3D7 gDNA and cloned into pSLI-sandwich [63] using the NotI/MluI restriction site.

For endogenous C-terminal 2x-FKBP-GFP tagging using the SLI system [63] a homology region of 1044 bp for *Pfmyof* (PF3D7_1329100), was amplified using 3D7 gDNA and cloned into pSLI-2xFKBP-GFP [63] using the NotI/MluI restriction site.

For endogenous C-terminal 3xHA tagging using the SLI system [63] a homology region of 948-999 bp (999 bp for *Pfmca2* (PF3D7_1438400), 948 bp for *Pfmyof* (PF3D7_1329100)) was amplified using 3D7 gDNA and cloned into pSLI-3xHA [111] using the NotI/XhoI restriction site.

For generating *Pf*MCA2^{Y1344Stop}-GFP a 984 bp homology region was amplified using 3D7 gDNA and cloned into the pSLI-TGD plasmid [63] using NotI and MluI restriction sites.

For targeted gene disruption (TGD) a 429-617 bp (534 bp for *kic12* (PF3D7_1329500), 615 bp for *Pfkic11* (PF3D7_1142100), 617 bp for *Pfuis14* (PF3D7_0405700), 429 bp for *Pfvps51* (PF3D7_0103100)) was amplified using 3D7 gDNA and cloned into the pSLI-TGD plasmid [63] using NotI and MluI restriction sites.
All oligonucleotides used to generate DNA fragments as well as those used for genotyping PCRs are listed in table S2.
For co-localisation experiments the plasmids p40PX-mCherry [44], pmCherry-K13_DHODH^{nmd3} [26], ^{ama1}PhIL1mCherry [112] and pGRASPmCherry-BSD^{nmd3} [26] were used.

Transfection of *P. falciparum*

For transfection, Percoll-purified [109] parasites at late schizont stage were transfected with 50 µg plasmid DNA using Amaxa Nucleofector 2b (Lonza, Switzerland) as previously described [113]. Transfectants were selected using either 4 nM WR99210 (Jacobus Pharmaceuticals), 0.9 µM DSM1 [114] (BEI Resources) or 2 mg/ml for Blasticidin (BSD) (Invitrogen). In order to select for parasites carrying the genomic modification via the SLI system [63], G418 (ThermoFisher, USA) at a final concentration of 400 µg/mL was added to a culture with about 5 % parasitemia. The selection process and integration test were performed as previously described [63].

Imaging

All fluorescence images were captured using a Zeiss Axioskop 2plus microscope with a Hamamatsu Digital camera (Model C4742-95) or for confocal imaging an Olympus FluoView 1000 confocal microscope.
Microscopy of live parasite-infected erythrocytes was performed as previously described [115]. Approximately 5 µL of infected erythrocytes were added on a glass slide and covered with a cover slip. Nuclei were stained with 1 µg/mL Hoechst-33342 (Invitrogen) or 1µg/mL 4',6'-diamidine-2'-phenylindole dihydrochloride (DAPI) (Roche).
Immunofluorescence assays (IFA) were performed as previously described [111]. Asynchronous parasite cultures with 5% parasitemia were harvested, washed twice with PBS, air-dried as thin monolayers on 10-well slides (Thermo Fischer) and fixed in 100% acetone for 30 min at room temperature. After rehydration with PBS, the cells were incubated with primary antibody solution containing rabbit a-HA (1:500) (Cell Signalling) and rat a-RFP (1:500) (Chromotek) diluted in 3% BSA in PBS. After three wash steps with PBS, incubation with corresponding secondary antibodies (Molecular probes) was performed. Slides were sealed with a coverslip using mounting medium (Dako).

716 **Parasite proliferation assay**

717 For proliferation assays a flow cytometry based assay, adapted from previously
718 published assays [44,116], was performed to measure multiplication over five days.
719 For knock sideways experiments, the same culture was split into control and + 250 nM
720 rapalog at the start of the proliferation assay and growth of each of these two cultures
721 followed over the course of the assay. Each day parasite cultures were resuspended
722 and 20 µL samples were transferred to an Eppendorf tube. 80 µL RPMI containing
723 Hoechst-33342 and dihydroethidium (DHE) was added to obtain final concentrations
724 of 5 µg/mL and 4.5 µg/mL, respectively. Samples were incubated for 20 min (protected
725 from UV light) at room temperature, and parasitemia was determined using an LSRII
726 flow cytometer by counting 100,000 events using the FACSDiva software (BD
727 Biosciences).
728
729 **Immunoblotting**

730 Protein samples were resolved by SDS-PAGE and transferred to Amersham Protran
731 membranes (GE Healthcare) in a tankblot device (Bio-Rad) using transfer buffer
732 (0.192 M Glycine, 0.1% SDS, 25 mM Tris) with 20% methanol. Next, membranes were
733 blocked for 30 minutes with 5% skim milk, and incubated with primary antibodies
734 diluted in PBS containing 5% skim milk for 2h or overnight, followed by three washing
735 steps with PBS and 2h incubation with horseradish peroxidase-conjugated secondary
736 antibodies diluted in PBS containing 5% skim milk. Detection was perfomed using the
737 Clarity Western ECL kit (Bio-Rad), and signals were recorded with a ChemiDoc XRS
738 imaging system (Bio-Rad) equipped with Image Lab software 5.2 (Bio-Rad).
739 Antibodies were applied in the following dilutions: mouse a-GFP (1:1000) (Roche), rat
740 a-HA (1:2000) (Roche), rabbit anti-aldolase (1.2000) [117], goat α-rat (1:2000)
741 (Dianova), goat α-mouse (1:2000) (Dianova) and donkey α-rabbit (1:2000) (Dianova).
742
743 **Conditional inactivation via knock-sideways**

744 For knock-sideways cell lines were transfected with plasmids encoding the nuclear
745 mislocaliser (NLS-FRB-mCherry) ot the PPM mislocaliser (Lyn-FRB-mCherry) [63].
746 The knock-sideways approach was performed as described previously [63]. Briefly,
747 cultures were split into two 2-ml cultures of which one was supplemented with 250 nM
748 rapalog (Clontech). Mislocalisation of the target protein was verified by live-cell
749 microscopy.
750
751 **Ring stage survival assay (RSA)**

752 RSAs were done as described previously [23,26]. Schizonts were purified from an
753 asynchronous parasite culture using a percoll gradient [109] and were allowed to
754 invade fresh RBCs at 37°C for 3 hours after which they were synchronised with 5%

sorbitol [110] to obtain 0 - 3 hour old rings. These rings were washed 3 times with medium and challenged with 700 nM DHA for 6 hours. Afterwards, the cells were washed three times in RPMI medium and the parasites were grown for another 66 hours. Finally, Giemsa smears were prepared in order to determine the parasite survival rate (parasitemia of viable parasites after DHA compared to parasitemia of non-DHA treated control). 1% parasite survival rate was considered the threshold for *in vitro* ART resistance [23]. Number of cells counted are indicated in the corresponding Figure legends.

Vesicle accumulation assay

The vesicle accumulation assay was adapted from [44]. Briefly, the number of vesicles per parasite were determined based on DIC images of synchronised trophozoites. For this, parasite cultures were two times synchronised (6-8 hours apart) using 5% sorbitol [110], split into two 2ml dishes of which one received rapalog to a final concentration of 250 nM, while the other culture served as control without rapalog and then grown for 16-24 hours to obtain trophozoite stages. Parasites were imaged in the DIC channel and the vesicles in the DIC images were counted. The assay was performed blinded and in at least three independent experiments (n of analysed cells indicated in the corresponding Figure legend).

Bloated food vacuole assay / E64 hemoglobin uptake assay

The bloated food vacuole assay was performed as previously described [44]. Briefly, ring stage parasite cultures with an 8h time window were obtained using double 5% sorbitol synchronisation. Parasites were either split into two 2ml dishes of which one received rapalog to a final concentration of 250 nM, while the other culture served as control without rapalog for *Pf*KIC11 and *Pf*KIC12 (see experimental setup scheme in Figure S4C, S5D) and incubated at 37°C overnight, or first incubated at 37°C overnight and split at the start of the assay for *Pf*MyoF (see experimental setup scheme in Figure S3E). When parasites reached the young trophozoites stage, the medium was aspirated and 1 ml medium containing 33 mM E64 protease inhibitor (Sigma Aldrich) was added. The cells were cultured for 8 hours and then imaged. The DIC image was used for scoring bloated food vacuoles and determination of parasite and food vacuole size. For visualisation of bloated food vacuoles, the cells were stained with 4.5 mg/ml dihydroethidium (DHE) for 15 minutes at 37°C. The experiment was performed blinded and in three independent experiments.

Domain identification using AlphaFold.

The predicted protein structures of all known K13-compartment members were downloaded from the AlphaFold Protein Structure Database (alphafold.ebi.ac.uk) [72],

except for UBP1 which was not available. The structure for UBP1 was predicted in 6 parts, coving resides 1-640, 641-1280, 1281-1920, 1921-2560, 2561-2880 and 2881-3499 using ColabFold [118]. VAST searches (ncbi.nlm.nih.gov/Structure/VAST/vastsearch.html) [119] were performed on all structures. The top 3 hits for each protein and protein part where aligned with the search model using the PyMol command cealign (Schrödinger, USA). Similarities with RMSDs of under 5 Å over more than 60 amino acids are listed in the results. Domains that were not previously annotated in Interpro (as of April 2022) [80] or PlasmoDB v.57 [120] were considered as newly identified.

Software

Statistical analyses were performed with GraphPad Prism version 8 (GraphPad Software, USA), microscopy images were processed in Corel Photo-Paint X6-X8 (https://www.coreldraw.com) or Fiji [121], plasmids and oligonucleotides were designed using ApE [122]. Protein structures were analysed and visualized using PyMol (Schrödinger, USA). Figures were arranged in CorelDraw X6-8.

Acknowledgements

We thank Jacobus Pharmaceuticals for WR99210. DSM1 (MRA-1161) was obtained from MR4/BEI Resources, NIAID, NIH. We thank Tim Gilberger for providing the PhIL1mcherry plasmid.

Author contribution

Conceptualization: TS
Validation: CCP
Formal Analysis: JSWM, SS, HB, TS
Investigation: JSWM, SS, HB, JB, IH, EJ, SS, SF
Resources: JB, EJ, SF, TS
Writing – original Draft: JSWM, HB, TS
Writing – Review & Editing: JSWM, HB, IH, TS
Visualization: JSWM, SS, HB, IH, TS
Supervision: TS
Funding Acquisition: TS
All authors read and approved the manuscript.
The authors declare that they have no conflict of interest.

Funding

HMB acknowledges funding by the Ortrud Mührer Fellowship of the Vereinigung der Freunde des Tropeninstituts Hamburg e.V, CCP thanks DAAD for funding. This work was funded by the European Research Council (ERC, grant 101021493).

Figures:

Table 1: Selection of putative K13 compartment proteins for further characterization in this manuscript

Figure 1: MCA2 is part of the K13 compartment and its truncation reduces ART susceptibility

(A) Schematic representation and nomenclature of MCA2 fusion proteins (not to scale) expressed in the parasite by modification of the endogenous gene. GFP in green, 3xHA in red and metacaspsase domain in grey. Amino acid positions are indicated by numbers. **(B)** Localisation of MCA2^{Y1344STOP}-GFP by live-cell microscopy across the intra-erythrocytic development cycle. Nuclei were stained with DAPI. Scale bar, 5 µm. (**C)** Live cell microscopy images of parasites expressing the truncated MCA2^{Y1344STOP}-GFP fusion protein with an episomally expressed mCherry-K13 fusion protein. Foci were categorized into ‘overlap’ (black), ‘partial overlap’ (dark grey) and ‘no overlap’ (light grey) and shown as frequencies in the pie chart (n = 46 cells were scored from a total of three independent experiments). **(D)** Live cell microscopy images of parasites expressing the truncated MCA2^{Y1344STOP}-GFP fusion protein with the IMC marker protein PhIL1mCherry. Zoom, enlarged region (factor 400%). **(E)** Relative growth of MCA2^{Y1344STOP} compared with 3D7 wild type parasites after two growth cycles. Each dot shows one of four independent experiments. P-values determined by one-sample t-test. **(F)** Parasite survival rate (% survival compared with control without DHA) 66 h after 6 h DHA treatment in standard RSA. Two (3D7) or three (MCA2 ^{Y1344STOP}) independent experiments, p-value determined by unpaired t-test. Green dashed line indicates 1% ART resistance cut-off [23]; 3419-3828 (mean 3632) erythrocytes for control and 10364-11734 (mean 11254) cells for DHA treated samples were counted. Nuclei were stained with DAPI (B) or Hoechst-33342 (D); scale bars, 5 µm and for zoom 1 µm.

Figure 2: MyoF is involved in host cell cytosol uptake and associated with the K13 compartment

(A) Localisation of MyoF-2xFKBP-GFP-2xFKBP expressed from the endogenous locus by live-cell microscopy across the intra-erythrocytic development cycle. Nuclei were stained with DAPI. **(B)** Live cell microscopy images of parasites expressing the

MyoF-2xFKBP-GFP-2xFKBP fusion protein with an episomally expressed FV marker P40PX-mCherry. **(C)** Live cell microscopy images of parasites expressing the MyoF-2xFKBP-GFP-2xFKBP fusion protein with episomally expressed mCherry-K13. Foci were categorized into 'overlap' (black), 'partial overlap' (dark grey), 'close foci' (=less than one focus radius apart) (light blue) and 'non overlap' (light grey). Three independent live microscopy sessions with each n=14 analysed parasites. **(D)** Relative growth of MyoF-2xFKBP-GFP-2xFKBP^{endo} compared with 3D7 wild type parasites after two growth cycles. Each dot shows one of four independent growth experiments. P-values determined by one-sample t-test. **(E)** Live-cell microscopy of knock sideways (rapalog) and control MyoF-2xFKBP-GFP-2xFKBP^{endo}+1xNLSmislocaliser parasites 1 hour or 22 hours after the induction by addition of rapalog. **(F)** Relative growth of 3D7 and MyoF-2xFKBP-GFP-2xFKBP^{endo}+1xNLSmislocaliser parasites (+ rapalog) compared with the corresponding control parasites (without rapalog) after two growth cycles. Three (3D7) and eight (MyoF-2xFKBP-GFP-2xFKBP^{endo}) independent experiments (individual experiments shown in Figure S3D). Error bars, mean ± SD. P-values determined by Welch's t-test. **(G)** Number of vesicles per parasite in trophozoites determined by live-cell fluorescence microscopy (DIC) in 3D7 and MyoF-2xFKBP-GFP-2xFKBP^{endo}+1xNLSmislocaliser parasites with and without rapalog addition. Three (3D7) and six (MyoF-2xFKBP-GFP-2xFKBP^{endo}+1xNLSmislocaliser) independent experiments with each time n=16-25 (mean 20.9) parasites analysed per condition. Mean of each independent experiment indicated by coloured triangle, individual datapoints by grey dots. Data presented according to SuperPlot guidelines [123]; Error bars represent mean ± SD. P-value for ± rapalog determined by paired t-test and for 3D7 vs MyoF by Mann-Whitney. Representative DIC images are displayed. **(H)** Bloated food vacuole assay with MyoF-2xFKBP-GFP-2xFKBP^{endo} parasites 8 hours after inactivation of MyoF (+ rapalog) compared with controls (-rapalog). Cells were categorized as with 'bloated FV' or 'non-bloated FV' and percentage of cells with bloated FV is displayed; n = 4 independent experiments with each n=33-40 (mean 34.6) parasites analysed per condition. P-values determined by Welch's t-test. Representative DIC and fluorescence microscopy images shown on the right. Parasite cytoplasm was visualized with DHE. Experimental setup shown in Figure S3E. **(I)** Parasite survival rate (% survival compared to control without DHA) 66 h after 6 h DHA (700 nM) treatment in standard RSA. MyoF-2xFKBP-GFP-2xFKBP^{endo} parasites + 1xNLSmislocaliser were pre-treated with rapalog either 12 or 24 hours prior to the assay. Three independent experiments, P-value determined by Wilcoxon test. Green dashed line indicates 1% ART resistance cut-off [23]. 2988-8392 (mean 5102) cells for control and 22704-44038 (mean 32077) cells for DHA treated samples were counted. Experimental setup shown in Figure S3F. Scale bars, 5 µm.

Figure 3: KIC11 is a K13 compartment protein important for asexual parasite proliferation, but not involved in endocytosis or *in vitro* ART resistance

(A) Localisation of KIC11-2xFKBP-GFP-2xFKBP expressed from the endogenous locus by live-cell microscopy across the intra-erythrocytic development cycle. (**B)** Live cell microscopy images of parasites expressing KIC11-2xFKBP-GFP-2xFKBP with episomally expressed mCherry-K13. White arrowheads indicate overlapping foci. Nuclei were stained with DAPI. Scale bar, 5 µm. **(C)** Live-cell microscopy of knock sideways (+ rapalog) and control (without rapalog) KIC11-2xFKBP-GFP-2xFKBP^{endo}+1xNLSmislocaliser parasites 4 and 16 hours after the induction of knock-sideways by addition of rapalog. Scale bar, 5 µm. **(D)** Relative growth of KIC11-2xFKBP-GFP-2xFKBP^{endo}+1xNLSmislocaliser (blue) and KIC11-2xFKBP-GFP-2xFKBP^{endo}+ LYNmislocaliser (red) plus rapalog compared with control parasites over two growth cycles. Five independent experiments were performed (depicted by different symbols) and mean relative parasitemia ± SD is shown (individual experiments shown in Figure S4A). **(E)** Parasite stage distribution in Giemsa smears at the time points (average hours post invasion, h) indicated above each bar in tightly synchronised (±4h) KIC11-2xFKBP-GFP-2xFKBP^{endo}+1xNLSmislocaliser parasites (rapalog addition at 4 hpi, 20 hpi, or 32 hpi and control) assayed over two consecutive cycles (last time point in cycle 3). A second replicate is shown in Figure S4B. **(F)** Giemsa smears of control and at 4 hpi, 20 hpi, or 32 hpi rapalog-treated KIC11-2xFKBP-GFP-2xFKBP^{endo}+1xNLSmislocaliser parasites shown in (E). **(G)** Number of vesicles per parasite in trophozoites determined by live-cell fluorescence microscopy (DIC) in KIC11-2xFKBP-GFP-2xFKBP^{endo}+1xNLSmislocaliser parasites with and without rapalog. Four independent experiments with n=16-59 (mean 30.1) parasites analysed per condition per experiment. Mean of each independent experiment indicated by coloured triangle, individual datapoints by grey dots. Data presented according to SuperPlot guidelines [123]; Error bars represent mean ± SD. P-value determined by paired t-test. Representative DIC images are displayed. **(H)** Bloated food vacuole assay with KIC11-2xFKBP-GFP-2xFKBP^{endo} parasites 8 hours after inactivation of KIC11 (+rapalog) compared with control (without rapalog). Cells were categorized as with ‘bloated FV’ or ‘non-bloated FV’ and displayed as percentage of cells with bloated FV; n=3 independent experiments with each n=19-36 (mean 26.5) parasites analysed per condition. P-values determined by Welch’s t-test. Representative DIC and fluorescence microscopy images are shown in the right panel. Parasite cytoplasm was visualized with DHE. Experimental setup shown in Figure S4C. **(I)** Parasite survival rate (% survival compared to control without DHA) 66 h after 6 h DHA treatment in standard RSA. Three independent experiments, P-value determined by paired t-test. Green dashed line indicates 1% ART resistance cut-off [23]. 2896-7135 (mean 4502) cells for control and 23183-32455 (mean 28496) cells

for DHA treated samples were counted. Experimental setup shown in Figure S4D. Nuclei were stained with DAPI (A, B). Scale bars, 5 µm.

Figure 4: KIC12 shows a dual localisation in the nucleus and at the K13 compartment and is involved in endocytosis but not in ART resistance

(A) Localisation of KIC12-2xFKBP-GFP-2xFKBP expressed from the endogenous locus by live-cell microscopy across the intra-erythrocytic development cycle. Arrow heads indicate foci (white) and nuclear (light blue) signal. (**B)** Live cell microscopy images of parasites expressing KIC12-2xFKBP-GFP-2xFKBP with episomally expressed mCherry-K13. Black arrowheads indicate overlapping foci. Nuclei were stained with DAPI. Scale bar, 5 µm. Extended panel shown in Figure S5A. **(C)** Live-cell microscopy of knock sideways (+ rapalog) and control (without rapalog) KIC12-2xFKBP-GFP-2xFKBP^{endo}+1xNLSmislocaliser parasites 4 and 16 hours after the induction of knock-sideways by addition of rapalog. **(D)** Relative growth of KIC12-2xFKBP-GFP-2xFKBP^{endo}+1xNLSmislocaliser (blue) and KIC12-2xFKBP-GFP-2xFKBP^{endo}+Lyn-mislocaliser (red) parasites plus rapalog compared with the corresponding untreated control parasites over two growth cycles. Five independent growth experiments were performed and mean relative parasitemia +/- SD is shown (all replicas shown in Figure S5B and C). **(E)** Live-cell microscopy of knock sideways (+ rapalog) and control (without rapalog) KIC12-2xFKBP-GFP-2xFKBP^{endo}+Lyn-mislocaliser parasites 4 hours after the induction of knock-sideways by addition of rapalog. **(F)** Bloated food vacuole assay with KIC12-2xFKBP-GFP-2xFKBP^{endo} parasites 8 hours after inactivation of KIC12 (+rapalog) by NLS-mislocaliser or Lyn-mislocaliser compared with corresponding control (without rapalog). Cells were categorized as ‘bloated FV’ and ‘non-bloated FV’. Results are displayed as percentage of cells with bloated FV. n=3 (NLS) or n=4 (LYN) independent experiments were performed with each n=19-80 (mean 41.3) parasites analysed per condition. P-values determined by Welch’s t-test. Representative DIC and fluorescence microscopy images are shown in the right panel. Parasite cytoplasm was visualized with DHE. Experimental setup shown in Figure S5D. Scale bar, 5 µm. **(G/I)** Area of the FV, area of the parasite and area of FV divided by area of the corresponding parasite of the FV of KIC12-2xFKBP-GFP-2xFKBP^{endo}+1xNLSmislocaliser (G) and KIC12-2xFKBP-GFP-2xFKBP^{endo}+LYNmislocaliser (I) parasites analysed in 4F. Mean of each independent experiment indicated by coloured triangle, individual datapoints by grey dots. Data presented according to SuperPlot guidelines [123]; Error bars represent mean ± SD. P-value determined by paired t-test. **(H/J)** Area of FV of individual cells plotted versus the area of the corresponding parasite in KIC12-2xFKBP-GFP-2xFKBP^{endo}+1xNLSmislocaliser and KIC12-2xFKBP-GFP-2xFKBP^{endo}+Lyn-mislocaliser parasites of the experiments shown in (F,G and I). Line represents linear

regression with error indicated by dashed line. Ten representative DIC images of each independent experiment are shown in Figure S5E,F **(K)** Number of vesicles per parasite in trophozoites determined by live-cell fluorescence microscopy (DIC) in KIC12-2xFKBP-GFP-2xFKBP^{endo}+1xNLSmislocaliser and KIC12-2xFKBP-GFP-2xFKBP^{endo}+Lyn-mislocaliser parasites with and without rapalog addition. Three independent experiments with n=10-56 (mean 28) parasites analysed per condition and experiment Data presented according to SuperPlot guidelines [123]; Mean of each independent experiment indicated by coloured triangle, individual datapoints by grey dots. Error bars represent mean ± SD. P-value determined by paired t-test. Representative DIC images are displayed. **(L)** Parasite survival rate (% survival compared to control without DHA) 66 h after 6 h DHA treatment in standard RSA. Three independent experiments, P-value determined by paired t-test. Green dashed line indicates 1% ART resistance cut-off [23]. 3151-4273 (mean 3690) cells for control and 6209-18941 (mean 12290) cells for DHA treated samples were counted. Nuclei were stained with DAPI (A, B). Experimental setup shown in Figure S5G.Scale bars, 5 µm.

Figure 5: Type of domain found in K13 compartment proteins coincide with functional group

(A) K13-compartment members shown to scale with domains indicated that were identified from AlphaFold structure predictions. Newly identified domains (i.e. domains not previously identified by sequence homology) are shown in colours, previously known domains are shown in grey. A brief summary of the function of each newly identified domain and Interpro IDs of all domains can be found in supplementary figure S8. **(B)** Alphafold prediction of each newly identified domain is shown in the same colour as in A and aligned with the most similar domain from the PDB. PDB ID and alignment details are indicated beneath each set of aligned domains. Root mean square deviations (RMSD) for all comparisons are given. **(C)** Domain organizations of human GGA1 (hGGA1), KIC4 and human AP-2 subunit beta 1 (hAP2B1) are shown (not to scale). Domains are coloured as in A and B. **(D)** Domain organizations of KIC5 and human AP-2 subunit alpha 1 (hAP2A1) are shown (not to scale). Domains are coloured as in A, B and C. (**E**) Table summarising K13 compartment proteins according to property (presence of vesicle trafficking domain (VTD)) and function.

Figure S1: Validation of generated transgenic cell lines

Confirmatory PCR of unmodified wildtype (WT) and transgenic knock-in (KI) / targeted-gene-disruption (TGD) cell lines to confirm correct genomic integration at the 3'- and 5'-end of the locus. Oligonucleotides used are listed in Table S2. **(A)** MCA2^{Y1344STOP}-GFP^{endo}; **(B)** MCA2-3xHA^{endo}; **(C)** MyoF-2xFKBP-GFP-2xFKBP^{endo}; **(D)** MyoF-

2xFKBP-GFP^{endo}; **(E)** MyoF-3xHA^{endo}; **(F)** KIC11-2xFKBP-GFP-2xFKBP^{endo}; **(G)** KIC12-2xFKBP-GFP-2xFKBP^{endo}; **(H)** PF3D7_0907200-2xFKBP-GFP-2xFKBP^{endo}; **(I)** VPS51-2xFKBP-GFP-2xFKBP^{endo}; **(J)** PF3D7_1365800-2xFKBP-GFP-2xFKBP^{endo}; **(K)** UIS14-2xFKBP-GFP-2xFKBP^{endo}; **(L)** PF3D7_1447800-2xFKBP-GFP-2xFKBP^{endo}; **(M)** VPS51-TGD^{endo}; **(N)** UIS14-TGD^{endo}. Right panel in **(A and B)** Western Blot analysis of **(A)** MCA2^{Y1344STOP}-GFP^{endo} cell line using mouse anti-GFP to detect the tagged fusion protein (upper panel) and rabbit anti-aldolase to control for equal loading (lower panel)(expected molecular weight for MCA2^{Y1344STOP}-GFP fusion proteins: 187 kDa) and **(B)** wildtype (3D7) and knock-in MCA2-3xHA^{endo} cell line using mouse anti-HA to detect the tagged full-length protein (upper panel) and rabbit anti-aldolase to control for equal loading (lower panel) (expected molecular weight for MCA2-3xHA fusion protein: 281 kDa). Protein size is indicated in kDa.

Figure S2: Additional data for MCA2

(A) Localisation of truncated the MCA2TGD-GFP by live-cell microscopy across the intra-erythrocytic development cycle. Nuclei were stained with DAPI. Scale bar, 5 µm. **(B)** IFA microscopy images of acetone-fixed parasites expressing MCA2-3xHA with episomally expressed mCherry-K13 across the intra-erythrocytic development cycle. Nuclei were stained with DAPI. Scale bar, 5µm. Foci were categorized into ‘overlap’ (black), ‘partial overlap’ (dark grey) and ‘no overlap’ (light grey) in n=30 parasites. Schematic representation of the cell lines depicted above the corresponding panel.

Figure S3: Additional data for MyoF

(A) Localisation of MyoF-2xFKBP-GFP by live-cell microscopy across the intra-erythrocytic development cycle. Nuclei were stained with DAPI. Scale bar, 5 µm. **(B)** IFA microscopy images of acetone-fixed parasites expressing MyoF-3xHA with episomally expressed mCherry-K13 across the intra-erythrocytic development cycle. Nuclei were stained with DAPI. Scale bar, 5µm. Foci were categorized into ‘overlap’ (black), ‘partial overlap’ (dark grey), close foci (light blue) and ‘non overlap’ (light grey) in n=31 parasites. Scale bar, 5µm. **(C)** Live-cell microscopy of knock sideways (+ rapalog) and control (without rapalog) MyoF-2xFKBP-GFP-2xFKBP^{endo}+1xNLSmislocaliser parasites at 0, 1, 2, 4 and 22 hours after the induction of knock-sideways by addition of rapalog. **(D)** Individual growth curves of MyoF-2xFKBP-GFP-2xFKBP^{endo}+1xNLSmislocaliser with (red) or without (blue) addition of rapalog shown in Figure 2F. **(E)** Experimental setup of the bloated food vacuole assay shown in Figure 2H. **(F)** Experimental setup of the RSA shown in Figure 2I. Schematic representation of the cell lines depicted above the corresponding panel.

Figure S4: Additional data for KIC11

(A) Individual growth curves of knock sideways (+ rapalog) and control (without rapalog) of KIC11-2xFKBP-GFP-2xFKBP^{endo}+1xNLSmislocaliser shown in Figure 3D. **(B)** Parasite stage distribution in Giemsa smears at the time points (average hours post invasion, h) indicated above each bar in tightly synchronised (±4h) KIC11-2xFKBP-GFP-2xFKBP^{endo}+1xNLSmislocaliser parasites (rapalog addition at 4 hpi, 20 hpi, or 32 hpi and control) parasite cultures over two consecutive cycles (last time point in cycle 3). A second replicate is shown in Figure 3E. **(C)** Experimental setup of the bloated food vacuole assay shown in Figure 3H. **(D)** Experimental setup of the RSA shown in Figure 3I. Schematic representation of the cell lines depicted above the corresponding panel.

Figure S5: Additional data for KIC12

(A) Localisation of KIC12-2xFKBP-GFP-2xFKBP by live-cell microscopy across the intra-erythrocytic development cycle. Nuclei were stained with DAPI. Scale bar, 5 µm. Expanded panel of Figure 4A **(B)** Individual growth curves of knock sideways (+ rapalog; red) and control (without rapalog; blue) KIC12-2xFKBP-GFP-2xFKBP^{endo}+1xNLSmislocaliser shown in Figure 4D. **(C)** Individual growth curves of knock sideways (+ rapalog; red) and control (without rapalog; blue) KIC12-2xFKBP-GFP-2xFKBP^{endo}+LYNmislocaliser shown in Figure 4D. **(D)** Experimental setup of the bloated food vacuole assay shown in Figure 4F-G. **(E)** Representative images of bloated food vacuole assay knock sideways (+ rapalog; bottom row) and control (without rapalog; top row) KIC12-2xFKBP-GFP-2xFKBP^{endo}+1xNLSmislocaliser Scale bar, 5 µm. **(F)** Representative images of knock sideways (+ rapalog, top row) and control (without rapalog; bottom row) KIC12-2xFKBP-GFP-2xFKBP^{endo}+LYNmislocaliser parasites from bloated food vacuole assay. Scale bar, 5 µm. **(G)** Experimental setup of the RSA shown in Figure 4J. Schematic representation of the cell lines depicted above the corresponding panel.

Figure S6: Candidate proteins not associated with the K13 compartment

(A) Live cell microscopy images of parasites endogenously expressing VPS51-2xFKBP-GFP-2xFKBP with episomally expressed mCherry-K13 across the intra-erythrocytic development cycle. Scale bar, 5 µm. **(B)** Localisation of truncated VPS51TGD-GFP fusion protein by live-cell microscopy across the intra-erythrocytic development cycle. Nuclei were stained with DAPI. Scale bar, 5 µm. Schematic representation of the truncation strategy depicted above the panel, numbers indicating AA. **(C)** Relative growth of VPS51TGD and UIS14TGD parasites compared to 3D7 wild type parasites after two cycles. Four independent growth experiments. P-values determined by one-sample t-test. **(D)** Live cell microscopy images of parasites endogenously expressing UIS14-2xFKBP-GFP-2xFKBP with episomally expressed

mCherry-K13 across the intra-erythrocytic development cycle. Scale bar, 5 µm. **(E)** Localisation of truncated UIS14TGD-GFP fusion protein by live-cell microscopy across the intra-erythrocytic development cycle. Nuclei were stained with DAPI. Scale bar, 5 µm. Schematic representation of the truncation strategy depicted above the panel, numbers indicating AA. **(F)** Live cell microscopy images of parasites endogenously expressing PF3D7_1447800-2xFKBP-GFP-2xFKBP with episomally expressed mCherry-K13 across the intra-erythrocytic development cycle. Nuclei were stained with DAPI. Scale bar, 5 µm. **(G)** Live cell microscopy images of parasites endogenously expressing PF3D7_0907200-2xFKBP-GFP-2xFKBP with episomally expressed mCherry-K13 across the intra-erythrocytic development cycle. Scale bar, 5 µm. Schematic representation of relevant features of each cell line depicted above the corresponding panel.

Figure S7: 3D7_1365800 an AH domain containing protein is dispensable for asexual parasite development

(A) Live cell microscopy images of parasites endogenously expressing PF3D7_1365800-2xFKBP-GFP-2xFKBP by live-cell microscopy across the intra-erythrocytic development cycle. Nuclei were stained with DAPI. Scale bar, 5 µm. (**B)** Expression of PF3D7_1365800-2xFKBP-GFP-2xFKBP with episomally expressed mCherry-K13. Scale bar, 5 µm. **(C)** Live-cell microscopy of knock sideways (+ rapalog) and control (without rapalog) PF3D7_1365800-2xFKBP-GFP-2xFKBP^{endo}+1xNLSmislocaliser parasites 16 hours after the induction of knock-sideways by addition of rapalog. Scale bar, 5 µm. **(D)** Individual growth curves of PF3D7_1365800-2xFKBP-GFP-2xFKBP^{endo}+1xNLSmislocaliser with (red) or without (blue) addition of rapalog. Relative growth of knock sideways (+ rapalog) and control (without rapalog) PF3D7_1365800-2xFKBP-GFP-2xFKBP^{endo}+1xNLSmislocaliser parasites over two cycles. Three independent growth experiments were performed and mean relative parasitemia ± SD is shown. **(E)** Live cell microscopy images of parasites expressing PF3D7_1365800-2xFKBP-GFP-2xFKBP with episomally expressed Golgi marker GRASP-mCherry. Schematic representation of the cell lines depicted above the corresponding panel. Scale bar, 5 µm.

Figure S8: Type of domain found in K13 compartment proteins coincide with functional group

(A) Full domain names and Interpro domain numbers for each domain in Figure 5 with indication in which K13-compartment members these proteins occur. For each newly identified domain a brief summary of its reported function is given. Colours are as in Figure 5. **(B)** Full length AlphaFold predictions for each K13-compartment member in which new domains were identified. New domains are coloured as in A and Figure 5.

For UBP1 no prediction was available in the EMBL-AlphaFold database, and the structure was predicted in fragments as described in the methods. The predicted fragment containing the newly identified domain is shown. **(C)** Full length structure of PF3D7_1365800, with AH domain in green. PF3D7_1365800 AH domain in green aligned with the most similar domain from the PDB. PDB ID and alignment details are indicated beneath each set of aligned domains. Brief summary about the AH domain and its Interpro ID are given.

Table S1: Selection characteristics of putative K13 compartment proteins selected for further characterization in this manuscript

Table S2: Oligonucleotides used for cloning and diagnostic genotyping PCR

References

1. WHO. World Malaria Report 2020. 2020.
2. Weiss DJ, Lucas TCD, Nguyen M, Nandi AK, Bisanzio D, Battle KE, et al. Mapping the global prevalence, incidence, and mortality of Plasmodium falciparum, 2000–17: a spatial and temporal modelling study. Lancet. 2019;394: 322–331. doi:10.1016/S0140-6736(19)31097-9
3. WHO. WHO Guidelines for malaria. WHO Guidelines for malaria. 2021.
4. Dondorp AM, Nosten F, Yi P, Das D, Phyo AP, Tarning J, et al. Artemisinin Resistance in Plasmodium falciparum Malaria. N Engl J Med. 2009;361: 455–467. doi:10.1056/NEJMoa0808859
5. Ashley EA, Dhorda M, Fairhurst RM, Amaratunga C, Lim P, Suon S, et al. Spread of Artemisinin Resistance in *Plasmodium falciparum* Malaria. N Engl J Med. 2014;371: 411–423. doi:10.1056/NEJMoa1314981
6. Amaratunga C, Sreng S, Suon S, Phelps ES, Stepniewska K, Lim P, et al. Artemisinin-resistant Plasmodium falciparum in Pursat province, western Cambodia: A parasite clearance rate study. Lancet Infect Dis. 2012;12: 851–858. doi:10.1016/S1473-3099(12)70181-0
7. Duru V, Khim N, Leang R, Kim S, Domergue A, Kloeung N, et al. Plasmodium falciparum dihydroartemisinin-piperaquine failures in Cambodia are associated with mutant K13 parasites presenting high survival rates in novel piperaquine in vitro assays: Retrospective and prospective investigations. BMC Med. 2015;13. doi:10.1186/s12916-015-0539-5
8. Woodrow CJ, White NJ. The clinical impact of artemisinin resistance in Southeast Asia and the potential for future spread. FEMS Microbiology Reviews. Oxford University Press; 2017. pp. 34–48. doi:10.1093/femsre/fuw037
9. Uwimana A, Umulisa N, Venkatesan M, Svigel SS, Zhou Z, Munyaneza T, et al. Association of Plasmodium falciparum kelch13 R561H genotypes with delayed parasite clearance in Rwanda: an open-label, single-arm, multicentre, therapeutic efficacy study. Lancet Infect Dis. 2021;21: 1120–1128. doi:10.1016/S1473-3099(21)00142-0

10. Uwimana A, Legrand E, Stokes BH, Ndikumana JLM, Warsame M, Umulisa N, et al. Emergence and clonal expansion of in vitro artemisinin-resistant Plasmodium falciparum kelch13 R561H mutant parasites in Rwanda. Nat Med. 2020;26. doi:10.1038/s41591-020-1005-2

11. Spring MD, Lin JT, Manning JE, Vanachayangkul P, Somethy S, Bun R, et al. Dihydroartemisinin-piperaquine failure associated with a triple mutant including kelch13 C580Y in Cambodia: An observational cohort study. Lancet Infect Dis. 2015;15: 683–691. doi:10.1016/S1473-3099(15)70049-6

12. Miotto O, Sekihara M, Tachibana SI, Yamauchi M, Pearson RD, Amato R, et al. Emergence of artemisinin-resistant Plasmodium falciparum with kelch13 C580Y mutations on the island of New Guinea. PLoS Pathog. 2020;16: e1009133. doi:10.1371/journal.ppat.1009133

13. Noedl H, Se Y, Schaecher K, Smith BL, Socheat D, Fukuda MM. Evidence of Artemisinin-Resistant Malaria in Western Cambodia. N Engl J Med. 2008;359: 2619–2620. doi:10.1056/NEJMc0805011

14. Mathieu LC, Cox H, Early AM, Mok S, Lazrek Y, Paquet JC, et al. Local emergence in amazonia of plasmodium falciparum K13 C580Y mutants associated with in vitro artemisinin resistance. Elife. 2020;9: 1–21. doi:10.7554/eLife.51015

15. Wasakul V, Disratthakit A, Mayxay M, Chindavongsa K, Sengsavath V, Thuy-Nhien N, et al. Malaria outbreak in Laos driven by a selective sweep for Plasmodium falciparum kelch13 R539T mutants: a genetic epidemiology analysis. Lancet Infect Dis. 2022;0. doi:10.1016/S1473-3099(22)00697-1

16. Phyo AP, Nkhoma S, Stepniewska K, Ashley EA, Nair S, McGready R, et al. Emergence of artemisinin-resistant malaria on the western border of Thailand: a longitudinal study. Lancet. 2012;379: 1960–1966. doi:10.1016/S0140-6736(12)60484-X

17. Klonis N, Xie SC, McCaw JM, Crespo-Ortiz MP, Zaloumis SG, Simpson JA, et al. Altered temporal response of malaria parasites determines differential sensitivity to artemisinin. Proc Natl Acad Sci U S A. 2013;110: 5157–5162. doi:10.1073/pnas.1217452110

18. Saralamba S, Pan-Ngum W, Maude RJ, Lee SJ, Tarning J, Lindegårdh N, et al. Intrahost modeling of artemisinin resistance in Plasmodium falciparum. Proc Natl Acad Sci U S A. 2011;108: 397–402. doi:10.1073/pnas.1006113108

19. Saunders DL, Vanachayangkul P, Lon C. Dihydroartemisinin–Piperaquine Failure in Cambodia. N Engl J Med. 2014;371: 484–485. doi:10.1056/nejmc1403007

20. Amaratunga C, Lim P, Suon S, Sreng S, Mao S, Sopha C, et al. Dihydroartemisinin-piperaquine resistance in Plasmodium falciparum malaria in Cambodia: A multisite prospective cohort study. Lancet Infect Dis. 2016;16: 357–365. doi:10.1016/S1473-3099(15)00487-9

21. Thanh NV, Thuy-Nhien N, Tuyen NTK, Tong NT, Nha-Ca NT, Dong LT, et al. Rapid decline in the susceptibility of Plasmodium falciparum to dihydroartemisinin-piperaquine in the south of Vietnam. Malar J. 2017;16: 1–10. doi:10.1186/s12936-017-1680-8

22. Watts RE, Odedra A, Marquart L, Webb L, Abd-Rahman AN, Cascales L, et al. Safety and parasite clearance of artemisinin-resistant Plasmodium falciparum

infection: A pilot and a randomised volunteer infection study in Australia. PLoS Med. 2020;17. doi:10.1371/JOURNAL.PMED.1003203

23. Witkowski B, Amaratunga C, Khim N, Sreng S, Chim P, Kim S, et al. Novel phenotypic assays for the detection of artemisinin-resistant Plasmodium falciparum malaria in Cambodia: In-vitro and ex-vivo drug-response studies. Lancet Infect Dis. 2013;13: 1043–1049. doi:10.1016/S1473-3099(13)70252-4

24. Ariey F, Witkowski B, Amaratunga C, Beghain J, Langlois AC, Khim N, et al. A molecular marker of artemisinin-resistant Plasmodium falciparum malaria. Nature. 2014;505: 50–55. doi:10.1038/nature12876

25. Straimer J, Gnädig NF, Witkowski B, Amaratunga C, Duru V, Ramadani AP, et al. K13-propeller mutations confer artemisinin resistance in Plasmodium falciparum clinical isolates. Science (80-). 2015;347: 428–431. doi:10.1126/science.1260867

26. Birnbaum J, Scharf S, Schmidt S, Jonscher E, Hoeijmakers WAM, Flemming S, et al. A Kelch13-defined endocytosis pathway mediates artemisinin resistance in malaria parasites. Science (80-). 2020;367: 51–59. doi:10.1126/science.aax4735

27. Yang T, Yeoh LM, Tutor M V., Dixon MW, McMillan PJ, Xie SC, et al. Decreased K13 Abundance Reduces Hemoglobin Catabolism and Proteotoxic Stress, Underpinning Artemisinin Resistance. Cell Rep. 2019;29: 2917-2928.e5. doi:10.1016/j.celrep.2019.10.095

28. Schumann R, Bischoff E, Klaus S, Möhring S, Flock J, Keller S, et al. Protein abundance and folding rather than the redox state of Kelch13 determine the artemisinin susceptibility of Plasmodium falciparum. Redox Biol. 2021;48. doi:10.1016/j.redox.2021.102177

29. Siddiqui G, Srivastava A, Russell AS, Creek DJ. Multi-omics based identification of specific biochemical changes associated with PfKelch13-mutant artemisinin-resistant plasmodium falciparum. J Infect Dis. 2017;215: 1435–1444. doi:10.1093/infdis/jix156

30. Mok S, Stokes BH, Gnädig NF, Ross LS, Yeo T, Amaratunga C, et al. Artemisinin-resistant K13 mutations rewire Plasmodium falciparum's intra-erythrocytic metabolic program to enhance survival. Nat Commun. 2021;12. doi:10.1038/s41467-020-20805-w

31. Behrens HM, Schmidt S, Spielmann T. The newly discovered role of endocytosis in artemisinin resistance. Med Res Rev. 2021; med.21848. doi:10.1002/med.21848

32. Francis SE, Sullivan DJ, Goldberg DE. Hemoglobin metabolism in the malaria parasite Plasmodium falciparium. Annual Review of Microbiology. Annual Reviews 4139 El Camino Way, P.O. Box 10139, Palo Alto, CA 94303-0139, USA; 1997. pp. 97–123. doi:10.1146/annurev.micro.51.1.97

33. Spielmann T, Gras S, Sabitzki R, Meissner M. Endocytosis in Plasmodium and Toxoplasma Parasites. Trends in Parasitology. Elsevier Ltd; 2020. pp. 520–532. doi:10.1016/j.pt.2020.03.010

34. Krugliak M, Zhang J, Ginsburg H. Intraerythrocytic Plasmodium falciparum utilizes only a fraction of the amino acids derived from the digestion of host cell cytosol for the biosynthesis of its proteins. Mol Biochem Parasitol. 2002;119: 249–256. doi:10.1016/S0166-6851(01)00427-3

35. Sherman IW. Amino acid metabolism and protein synthesis in malarial parasites. Bulletin of the World Health Organization. World Health Organization; 1977. pp. 265–276.

36. Matz JM. Plasmodium's bottomless pit: properties and functions of the malaria parasite's digestive vacuole. Trends in Parasitology. Elsevier Ltd; 2022. pp. 525–543. doi:10.1016/j.pt.2022.02.010

37. Mesén-Ramírez P, Bergmann B, Elhabiri M, Zhu L, Thien H von, Castro-Peña C, et al. The parasitophorous vacuole nutrient pore is critical for drug access in malaria parasites and modulates the fitness cost of artemisinin resistance. Cell Host Microbe. 2021;0: 283. doi:10.1016/j.chom.2021.11.002

38. Bunditvorapoom D, Kochakarn T, Kotanan N, Modchang C, Kümpornsin K, Loesbanluechai D, et al. Fitness Loss under Amino Acid Starvation in Artemisinin-Resistant Plasmodium falciparum Isolates from Cambodia. Sci Rep. 2018;8: 1–9. doi:10.1038/s41598-018-30593-5

39. Milani KJ, Schneider TG, Taraschi TF. Defining the morphology and mechanism of the hemoglobin transport pathway in Plasmodium falciparum-infected erythrocytes. Eukaryot Cell. 2015;14: 415–426. doi:10.1128/EC.00267-14

40. Bakar NA, Klonis N, Hanssen E, Chan C, Tilley L. Digestive-vacuole genesis and endocytic processes in the early intraerythrocytic stages of Plasmodium falciparum. J Cell Sci. 2010;123: 441–450. doi:10.1242/jcs.061499

41. Smythe WA, Joiner KA, Hoppe HC. Actin is required for endocytic trafficking in the malaria parasite Plasmodium falciparum. Cell Microbiol. 2008;10: 452–464. doi:10.1111/j.1462-5822.2007.01058.x

42. Zhou HC, Gao YH, Zhong X, Wang H. Dynamin like protein 1 participated in the hemoglobin uptake pathway of Plasmodium falciparum. Chin Med J (Engl). 2009;122: 1686–1691. doi:10.3760/cma.j.issn.0366-6999.2009.14.015

43. Taraschi TF, O'Donnell M, Martinez S, Schneider T, Trelka D, Fowler VM, et al. Generation of an erythrocyte vesicle transport system by Plasmodium falciparum malaria parasites. Blood. 2003;102: 3420–3426. doi:10.1182/blood-2003-05-1448

44. Jonscher E, Flemming S, Schmitt M, Sabitzki R, Reichard N, Birnbaum J, et al. PfVPS45 Is Required for Host Cell Cytosol Uptake by Malaria Blood Stage Parasites. Cell Host Microbe. 2019;25: 166-173.e5. doi:10.1016/j.chom.2018.11.010

45. Mukherjee A, Crochetière M-È, Sergerie A, Amiar S, Thompson LA, Ebrahimzadeh Z, et al. A Phosphoinositide-Binding Protein Acts in the Trafficking Pathway of Hemoglobin in the Malaria Parasite Plasmodium falciparum. Soldati-Favre D, editor. MBio. 2022;13. doi:10.1128/mbio.03239-21

46. Wagner MP, Formaglio P, Gorgette O, Dziekan JM, Huon C, Berneburg I, et al. Human peroxiredoxin 6 is essential for malaria parasites and provides a host-based drug target. Cell Rep. 2022;39: 110923. doi:10.1016/j.celrep.2022.110923

47. Roux KJ, Kim DI, Raida M, Burke B. A promiscuous biotin ligase fusion protein identifies proximal and interacting proteins in mammalian cells. J Cell Biol. 2012;196: 801–810. doi:10.1083/jcb.201112098

48. Kimmel J, Kehrer J, Frischknecht F, Spielmann T. Proximity-dependent

biotinylation approaches to study apicomplexan biology. Mol Microbiol. 2021. doi:10.1111/mmi.14815

49. Kono M, Herrmann S, Loughran NB, Cabrera A, Engelberg K, Lehmann C, et al. Evolution and architecture of the inner membrane complex in asexual and sexual stages of the malaria parasite. Mol Biol Evol. 2012;29: 2113–2132. doi:10.1093/molbev/mss081

50. Parkyn Schneider M, Liu B, Glock P, Suttie A, McHugh E, Andrew D, et al. Disrupting assembly of the inner membrane complex blocks Plasmodium falciparum sexual stage development. Gilberger TW, editor. PLOS Pathog. 2017;13: e1006659. doi:10.1371/journal.ppat.1006659

51. Saini E, Zeeshan M, Brady D, Pandey R, Kaiser G, Koreny L, et al. Photosensitized INA-Labelled protein 1 (PhIL1) is novel component of the inner membrane complex and is required for Plasmodium parasite development. Sci Rep. 2017;7: 15577. doi:10.1038/s41598-017-15781-z

52. Saini E, Sheokand PK, Sharma V, Agrawal P, Kaur I, Singh S, et al. Plasmodium falciparum PhIL1-associated complex plays an essential role in merozoite reorientation and invasion of host erythrocytes. PLOS Pathog. 2021;17: e1009750. doi:10.1371/JOURNAL.PPAT.1009750

53. Torres JA, Pasquarelli RR, Back PS, Moon AS, Bradley PJ. Identification and Molecular Dissection of IMC32, a Conserved Toxoplasma Inner Membrane Complex Protein That Is Essential for Parasite Replication. Boyle JP, editor. MBio. 2021;12. doi:10.1128/mBio.03622-20

54. Wichers JS, Wunderlich J, Heincke D, Pazicky S, Strauss J, Schmitt M, et al. Identification of novel inner membrane complex and apical annuli proteins of the malaria parasite Plasmodium falciparum. Cell Microbiol. 2021;23: e13341. doi:10.1111/cmi.13341

55. Rudlaff RM, Kraemer S, Streva VA, Dvorin JD. An essential contractile ring protein controls cell division in Plasmodium falciparum. Nat Commun. 2019;10: 2181. doi:10.1038/s41467-019-10214-z

56. Geiger M, Brown C, Wichers JS, Strauss J, Lill A, Thuenauer R, et al. Structural Insights Into PfARO and Characterization of its Interaction With PfAIP. J Mol Biol. 2020;432: 878–896. doi:10.1016/j.jmb.2019.12.024

57. Koreny L, Zeeshan M, Barylyuk K, Tromer EC, van Hooff JJE, Brady D, et al. Molecular characterization of the conoid complex in Toxoplasma reveals its conservation in all apicomplexans, including Plasmodium species. Duffy M, editor. PLOS Biol. 2021;19: e3001081. doi:10.1371/journal.pbio.3001081

58. Thommen BT, Dziekan JM, Achcar F, Tjia S, Passecker A, Buczak K, et al. FKBP35 secures ribosome homeostasis in Plasmodium falciparum. bioRxiv. 2022; 2022.12.09.519720. doi:10.1101/2022.12.09.519720

59. Kumar R, Adams B, Musiyenko A, Shulyayeva O, Barik S. The FK506-binding protein of the malaria parasite, Plasmodium falciparum, is a FK506-sensitive chaperone with FK506-independent calcineurin-inhibitory activity. Mol Biochem Parasitol. 2005;141: 163–73. doi:10.1016/j.molbiopara.2005.02.007

60. Boucher MJ, Ghosh S, Zhang L, Lal A, Jang SW, Ju A, et al. Integrative proteomics and bioinformatic prediction enable a high-confidence apicoplast proteome in malaria parasites. Striepen B, editor. PLoS Biol. 2018;16: e2005895. doi:10.1371/journal.pbio.2005895

61. MalariaGEN, Ahouidi A, Ali M, Almagro-Garcia J, Amambua-Ngwa A, Amaratunga C, et al. An open dataset of Plasmodium falciparum genome variation in 7,000 worldwide samples. Wellcome open Res. 2021;6: 42. doi:10.12688/wellcomeopenres.16168.2

62. Wichers JS, Tonkin-Hill G, Thye T, Krumkamp R, Kreuels B, Strauss J, et al. Common virulence gene expression in adult first-time infected malaria patients and severe cases. Elife. 2021;10. doi:10.7554/eLife.69040

63. Birnbaum J, Flemming S, Reichard N, Soares AB, Mesén-Ramírez P, Jonscher E, et al. A genetic system to study Plasmodium falciparum protein function. Nat Methods. 2017;14: 450–456. doi:10.1038/nmeth.4223

64. Lazarus MD, Schneider TG, Taraschi TF. A new model for hemoglobin ingestion and transport by the human malaria parasite Plasmodium falciparum. J Cell Sci. 2008;121: 1937–1949. doi:10.1242/jcs.023150

65. Wichers JS, Scholz JAM, Strauss J, Witt S, Lill A, Ehnold L-I, et al. Dissecting the Gene Expression, Localisation, Membrane Topology, and Function of the Plasmodium falciparum STEVOR Protein Family. Boothroyd JC, editor. MBio. 2019;10: e01500-19. doi:10.1128/mBio.01500-19

66. Subudhi AK, O'Donnell AJ, Ramaprasad A, Abkallo HM, Kaushik A, Ansari HR, et al. Malaria parasites regulate intra-erythrocytic development duration via serpentine receptor 10 to coordinate with host rhythms. Nat Commun. 2020;11. doi:10.1038/s41467-020-16593-y

67. Robinson MS, Sahlender DA, Foster SD. Rapid Inactivation of Proteins by Rapamycin-Induced Rerouting to Mitochondria. Dev Cell. 2010;18: 324–331. doi:10.1016/j.devcel.2009.12.015

68. Haruki H, Nishikawa J, Laemmli UK. The Anchor-Away Technique: Rapid, Conditional Establishment of Yeast Mutant Phenotypes. Mol Cell. 2008;31: 925–932. doi:10.1016/j.molcel.2008.07.020

69. Sijwali PS, Rosenthal PJ. Gene disruption confirms a critical role for the cysteine protease falcipain-2 in hemoglobin hydrolysis by Plasmodium falciparum. Proc Natl Acad Sci U S A. 2004;101: 4384–4389. doi:10.1073/pnas.0307720101

70. Otto TD, Wilinski D, Assefa S, Keane TM, Sarry LR, Böhme U, et al. New insights into the blood-stage transcriptome of Plasmodium falciparum using RNA-Seq. Mol Microbiol. 2010;76: 12–24. doi:10.1111/j.1365-2958.2009.07026.x

71. Kimmel J, Schmitt M, Sinner A, Jansen P, Mainye S, Ramón-Zamorano G, et al. Gene-by-gene screen of the unknown proteins encoded on P. falciparum chromosome 3. bioRxiv. 2022; 2022.07.07.499005. doi:10.1101/2022.07.07.499005

72. Jumper J, Evans R, Pritzel A, Green T, Figurnov M, Ronneberger O, et al. Highly accurate protein structure prediction with AlphaFold. Nature. 2021;596: 583–589. doi:10.1038/s41586-021-03819-2

73. Cherfils J. Structural mimicry of DH domains by Arfaptin suggests a model for the recognition of Rac-GDP by its guanine nucleotide exchange factors. FEBS Lett. 2001;507: 280–284. doi:10.1016/S0014-5793(01)02970-2

74. Tarricone C, Xiao B, Justin N, Walker PA, Rittinger K, Gamblin SJ, et al. The structural basis of Arfaptin-mediated cross-talk between Rac and Arf signalling

pathways. Nature. 2001;411: 215–219. doi:10.1038/35075620

75. McGovern OL, Rivera-Cuevas Y, Kannan G, Narwold AJ, Carruthers VB. Intersection of endocytic and exocytic systems in Toxoplasma gondii. Traffic. 2018;19: 336–353. doi:10.1111/tra.12556

76. Struck NS, de Souza Dias S, Langer C, Marti M, Pearce JA, Cowman AF, et al. Re-defining the Golgi complex in Plasmodium falciparum using the novel Golgi marker PfGRASP. J Cell Sci. 2005;118: 5603–5613. doi:10.1242/jcs.02673

77. Varadi M, Anyango S, Deshpande M, Nair S, Natassia C, Yordanova G, et al. AlphaFold Protein Structure Database: Massively expanding the structural coverage of protein-sequence space with high-accuracy models. Nucleic Acids Res. 2022;50: D439–D444. doi:10.1093/nar/gkab1061

78. Hirst J, Lui WWY, Bright NA, Totty N, Seaman MNJ, Robinson MS. A family of proteins with γ-adaptin and VHS domains that facilitate trafficking between the trans-golgi network and the vacuole/lysosome. J Cell Biol. 2000;149: 67–79. doi:10.1083/jcb.149.1.67

79. Dell'Angelica EC, Puertollano R, Mullins C, Aguilar RC, Vargas JD, Hartnell LM, et al. GGAs: A family of ADP ribosylation factor-binding proteins related to adaptors and associated with the Golgi complex. J Cell Biol. 2000;149: 81–93. doi:10.1083/jcb.149.1.81

80. Blum M, Chang HY, Chuguransky S, Grego T, Kandasaamy S, Mitchell A, et al. The InterPro protein families and domains database: 20 years on. Nucleic Acids Res. 2021;49: D344–D354. doi:10.1093/nar/gkaa977

81. Koreny L, Mercado-Saavedra BN, Klinger CM, Barylyuk K, Butterworth S, Hirst J, et al. Stable and ancient endocytic structures navigate the complex pellicle of apicomplexan parasites. bioRxiv. 2022; 2022.06.02.494549. doi:10.1101/2022.06.02.494549

82. Tanna CE, Goss LB, Ludwig CG, Chen PW. Arf GAPs as regulators of the actin cytoskeleton—An update. International Journal of Molecular Sciences. MDPI AG; 2019. doi:10.3390/ijms20020442

83. Kjos I, Vestre K, Guadagno NA, Borg Distefano M, Progida C. Rab and Arf proteins at the crossroad between membrane transport and cytoskeleton dynamics. Biochimica et Biophysica Acta - Molecular Cell Research. Elsevier B.V.; 2018. pp. 1397–1409. doi:10.1016/j.bbamcr.2018.07.009

84. Hunt P, Afonso A, Creasey A, Culleton R, Sidhu ABS, Logan J, et al. Gene encoding a deubiquitinating enzyme is mutated in artesunate- and chloroquine-resistant rodent malaria parasites. Mol Microbiol. 2007;65: 27–40. doi:10.1111/j.1365-2958.2007.05753.x

85. Sun D, Leung CL, Liem RK. Characterization of the microtubule binding domain of microtubule actin crosslinking factor (MACF): identification of a novel group of microtubule associated proteins. J Cell Sci. 2001;114: 161–172. doi:10.1242/jcs.114.1.161

86. Sahu SC, Swanson KA, Kang RS, Huang K, Brubaker K, Ratcliff K, et al. Conserved Themes in Target Recognition by the PAH1 and PAH2 Domains of the Sin3 Transcriptional Corepressor. J Mol Biol. 2008;375: 1444–1456. doi:10.1016/j.jmb.2007.11.079

87. Brubaker K, Cowley SM, Huang K, Loo L, Yochum GS, Ayer DE, et al.

Solution structure of the interacting domains of the mad-sin3 complex: Implications for recruitment of a chromatin-modifying complex. Cell. 2000;103: 655–665. doi:10.1016/S0092-8674(00)00168-9

88. Doherty GJ, McMahon HT. Mechanisms of Endocytosis. Annu Rev Biochem. 2009;78: 857–902. doi:10.1146/annurev.biochem.78.081307.110540

89. Kaksonen M, Roux A. Mechanisms of clathrin-mediated endocytosis. Nature Reviews Molecular Cell Biology. Nature Publishing Group; 2018. pp. 313–326. doi:10.1038/nrm.2017.132

90. Thottacherry JJ, Sathe M, Prabhakara C, Mayor S. Spoiled for choice: Diverse endocytic pathways function at the cell surface. Annual Review of Cell and Developmental Biology. Annual Reviews Inc.; 2019. pp. 55–84. doi:10.1146/annurev-cellbio-100617-062710

91. Henrici RC, Edwards RL, Zoltner M, van Schalkwyk DA, Hart MN, Mohring F, et al. The plasmodium falciparum artemisinin susceptibility-associated ap-2 adaptin μ subunit is clathrin independent and essential for schizont maturation. MBio. 2020;11. doi:10.1128/mBio.02918-19

92. Schmid EM, Ford MGJ, Burtey A, Praefcke GJK, Peak-Chew S-Y, Mills IG, et al. Role of the AP2 β-Appendage Hub in Recruiting Partners for Clathrin-Coated Vesicle Assembly. Hughson F, editor. PLoS Biol. 2006;4: e262. doi:10.1371/journal.pbio.0040262

93. Perrais D. Cellular and structural insight into dynamin function during endocytic vesicle formation: a tale of 50 years of investigation. Biosci Rep. 2022;42. doi:10.1042/bsr20211227

94. Heredero-Bermejo I, Varberg JM, Charvat R, Jacobs K, Garbuz T, Sullivan WJ, et al. TgDrpC, an atypical dynamin-related protein in *Toxoplasma gondii,* is associated with vesicular transport factors and parasite division. Mol Microbiol. 2019;111: 46–64. doi:10.1111/mmi.14138

95. Wall RJ, Zeeshan M, Katris NJ, Limenitakis R, Rea E, Stock J, et al. Systematic analysis of Plasmodium myosins reveals differential expression, localisation, and function in invasive and proliferative parasite stages. Cell Microbiol. 2019;21. doi:10.1111/cmi.13082

96. DePina AS, Langford GM. Vesicle transport: The role of actin filaments and myosin motors. Microsc Res Tech. 1999;47: 93–106. doi:10.1002/(SICI)1097-0029(19991015)47:2<93::AID-JEMT2>3.0.CO;2-P

97. Chakrabarti R, Lee M, Higgs HN. Multiple roles for actin in secretory and endocytic pathways. Current Biology. Cell Press; 2021. pp. R603–R618. doi:10.1016/j.cub.2021.03.038

98. Zhang M, Wang C, Otto TD, Oberstaller J, Liao X, Adapa SR, et al. Uncovering the essential genes of the human malaria parasite Plasmodium falciparum by saturation mutagenesis. Science. 2018;360: eaap7847. doi:10.1126/science.aap7847

99. Carmeille R, Schiano Lomoriello P, Devarakonda PM, Kellermeier JA, Heaslip AT. Actin and an unconventional myosin motor, TgMyoF, control the organization and dynamics of the endomembrane network in Toxoplasma gondii. Gubbels M-J, editor. PLOS Pathog. 2021;17: e1008787. doi:10.1371/journal.ppat.1008787

100. Jacot D, Daher W, Soldati-Favre D. Toxoplasma gondii myosin F, an essential

motor for centrosomes positioning and apicoplast inheritance. EMBO J. 2013;32: 1702–1716. doi:10.1038/emboj.2013.113

101. Kumari V, Prasad KM, Kalia I, Sindhu G, Dixit R, Rawat DS, et al. Dissecting the role of Plasmodium Metacaspase-2 in malaria gametogenesis and sporogony. Emerg Microbes Infect. 2022; 1–50. doi:10.1080/22221751.2022.2052357

102. Fonager J, Franke-Fayard BMD, Adams JH, Ramesar J, Klop O, Khan SM, et al. Development of the piggyBac transposable system for Plasmodium berghei and its application for random mutagenesis in malaria parasites. BMC Genomics. 2011;12. doi:10.1186/1471-2164-12-155

103. Kumari V, Singh AP, Singh J, Sharma R, Akhter M, Mishra PK, et al. Biochemical characterization of unusual cysteine protease of P. falciparum, metacaspase-2 (MCA-2). Mol Biochem Parasitol. 2018;220: 28–41. doi:10.1016/j.molbiopara.2018.01.001

104. Vandana, Shankar S, Prasad KM, Kashif M, Kalia I, Rai R, et al. A nonpeptidyl molecule modulates apoptosis-like cell death by inhibiting P. Falciparum metacaspase-2. Biochem J. 2020;477: 1323–1344. doi:10.1042/BCJ20200050

105. Vandana , Pandey R, Srinivasan E, Kalia I, Singh AP, Saxena A, et al. Plasmodium falciparum metacaspase-2 capture its natural substrate in a non-canonical way . J Biochem. 2021;170: 639–653. doi:10.1093/jb/mvab086

106. Bushell E, Gomes AR, Sanderson T, Anar B, Girling G, Herd C, et al. Functional Profiling of a Plasmodium Genome Reveals an Abundance of Essential Genes. Cell. 2017;170: 260-272.e8. doi:10.1016/j.cell.2017.06.030

107. Walliker D, Quakyi IA, Wellems TE, McCutchan TF, Szarfman A, London WT, et al. Genetic analysis of the human malaria parasite Plasmodium falciparum. Science (80-). 1987;236: 1661–6.

108. Trager W, Jensen JB. Continuous culture of Plasmodium falciparum: its impact on malaria research. Int J Parasitol. 1997;27: 989–1006. doi:10.1016/S0020-7519(97)00080-5

109. Rivadeneira E, Wasserman M, Espinal C. Separation and Concentration of Schizonts of Plasmodium falciparum by Percoll Gradients. J Protozool. 1983;30: 367–370. doi:10.1111/j.1550-7408.1983.tb02932.x

110. Lambros C, Vanderberg JP. Synchronization of Plasmodium falciparum Erythrocytic Stages in Culture. J Parasitol. 1979;65: 418. doi:10.2307/3280287

111. Mesén-Ramírez P, Bergmann B, Tran TT, Garten M, Stäcker J, Naranjo-Prado I, et al. EXP1 is critical for nutrient uptake across the parasitophorous vacuole membrane of malaria parasites. de Koning-Ward TF, editor. PLoS Biol. 2019;17: e3000473. doi:10.1371/journal.pbio.3000473

112. Wichers-Misterek JS, Binder AM, Mesén-Ramírez P, Dorner LP, Safavi S, Fuchs G, et al. A microtubule associated protein is essential for malaria parasite transmission. bioRxiv. 2022; 2022.10.18.512810. doi:10.1101/2022.10.18.512810

113. Moon RW, Hall J, Rangkuti F, Ho YS, Almond N, Mitchell GH, et al. Adaptation of the genetically tractable malaria pathogen Plasmodium knowlesi to continuous culture in human erythrocytes. Proc Natl Acad Sci. 2013;110: 531–536. doi:10.1073/pnas.1216457110

114. Ganesan SM, Morrisey JM, Ke H, Painter HJ, Laroiya K, Phillips MA, et al.

Yeast dihydroorotate dehydrogenase as a new selectable marker for Plasmodium falciparum transfection. Mol Biochem Parasitol. 2011;177: 29–34. doi:10.1016/j.molbiopara.2011.01.004

115. Grüring C, Spielmann T. Imaging of live malaria blood stage parasites. Methods Enzymol. 2012;506: 81–92. doi:10.1016/B978-0-12-391856-7.00029-9

116. Malleret B, Claser C, Ong ASM, Suwanarusk R, Sriprawat K, Howland SW, et al. A rapid and robust tri-color flow cytometry assay for monitoring malaria parasite development. Sci Rep. 2011;1: 118. doi:10.1038/srep00118

117. Mesén-Ramírez P, Reinsch F, Blancke Soares A, Bergmann B, Ullrich AK, Tenzer S, et al. Stable Translocation Intermediates Jam Global Protein Export in Plasmodium falciparum Parasites and Link the PTEX Component EXP2 with Translocation Activity. Soldati-Favre D, editor. PLoS Pathog. 2016;12: e1005618. doi:10.1371/journal.ppat.1005618

118. Mirdita M, Schütze K, Moriwaki Y, Heo L, Ovchinnikov S, Steinegger M. ColabFold: making protein folding accessible to all. Nat Methods. 2022;19: 679–682. doi:10.1038/s41592-022-01488-1

119. Gibrat JF, Madej T, Bryant SH. Surprising similarities in structure comparison. Curr Opin Struct Biol. 1996;6: 377–385. doi:10.1016/S0959-440X(96)80058-3

120. Aurrecoechea C, Brestelli J, Brunk BP, Dommer J, Fischer S, Gajria B, et al. PlasmoDB: a functional genomic database for malaria parasites. Nucleic Acids Res. 2009;37: D539–D543. doi:10.1093/nar/gkn814

121. Schindelin J, Arganda-Carreras I, Frise E, Kaynig V, Longair M, Pietzsch T, et al. Fiji: an open-source platform for biological-image analysis. Nat Methods. 2012;9: 676–682. doi:10.1038/nmeth.2019

122. Davis MW, Jorgensen EM. ApE, A Plasmid Editor: A Freely Available DNA Manipulation and Visualization Program. Front Bioinforma. 2022;2: 5. doi:10.3389/fbinf.2022.818619

123. Lord SJ, Velle KB, Mullins RD, Fritz-Laylin LK. SuperPlots: Communicating reproducibility and variability in cell biology. J Cell Biol. 2020;219. doi:10.1083/jcb.202001064

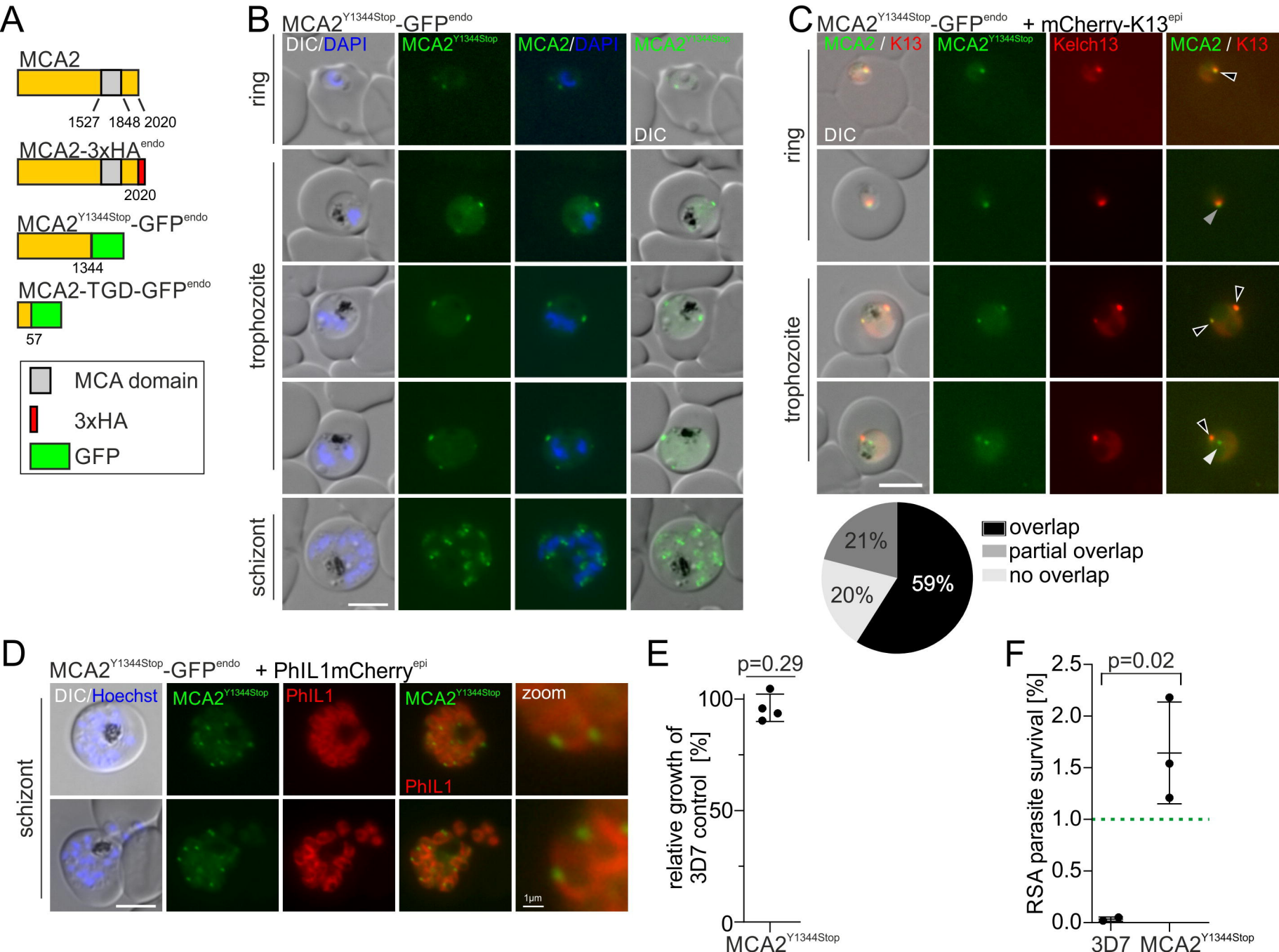
A
MCA2
1527 1848 2020
MCA2-3xHA endo
2020
MCA2 Y1344Stop -GFP endo
1344
MCA2-TGD-GFP endo
57
MCA domain
3xHA
GFP
B
MCA2 Y1344Stop -GFP endo
DIC/DAPI
MCA2 Y1344Stop
MCA2/DAPI
DIC
ring
trophozoite
schizont
C
MCA2 Y1344Stop -GFP endo + mCherry-K13 epi
MCA2 / K13
MCA2 Y1344Stop
Kelch13
DIC
ring
trophozoite
21%
59%
20%
overlap
partial overlap
no overlap
D
MCA2 Y1344Stop -GFP endo + PhIL1mCherry epi
DIC/Hoechst
MCA2 Y1344Stop
PhIL1
zoom
1µm
schizont
E
p=0.29
relative growth of 3D7 control [%]
100
50
0
MCA2 Y1344Stop
F
p=0.02
RSA parasite survival [%]
2.5
2.0
1.5
1.0
0.5
0.0
3D7
MCA2 Y1344Stop

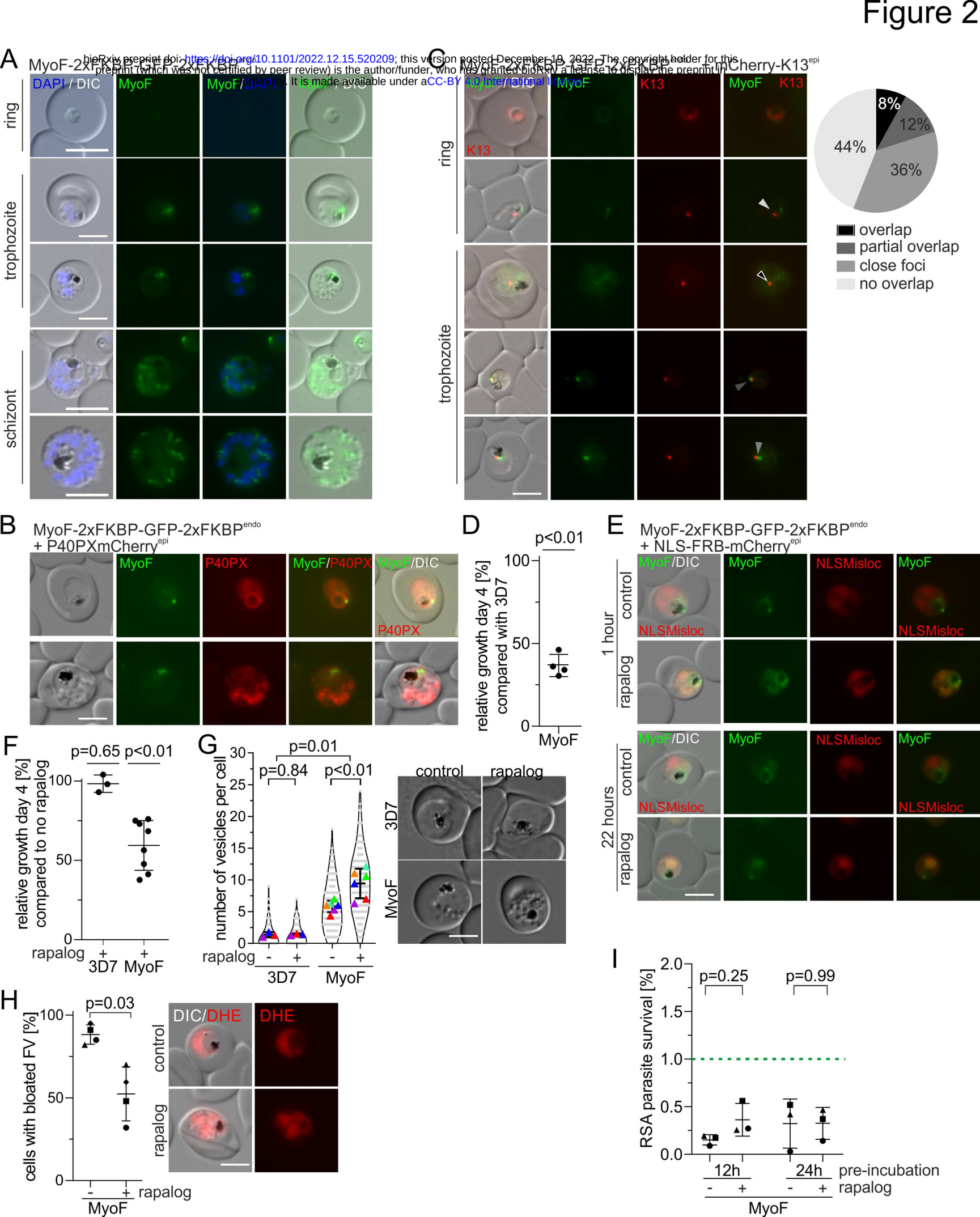

Figure 3

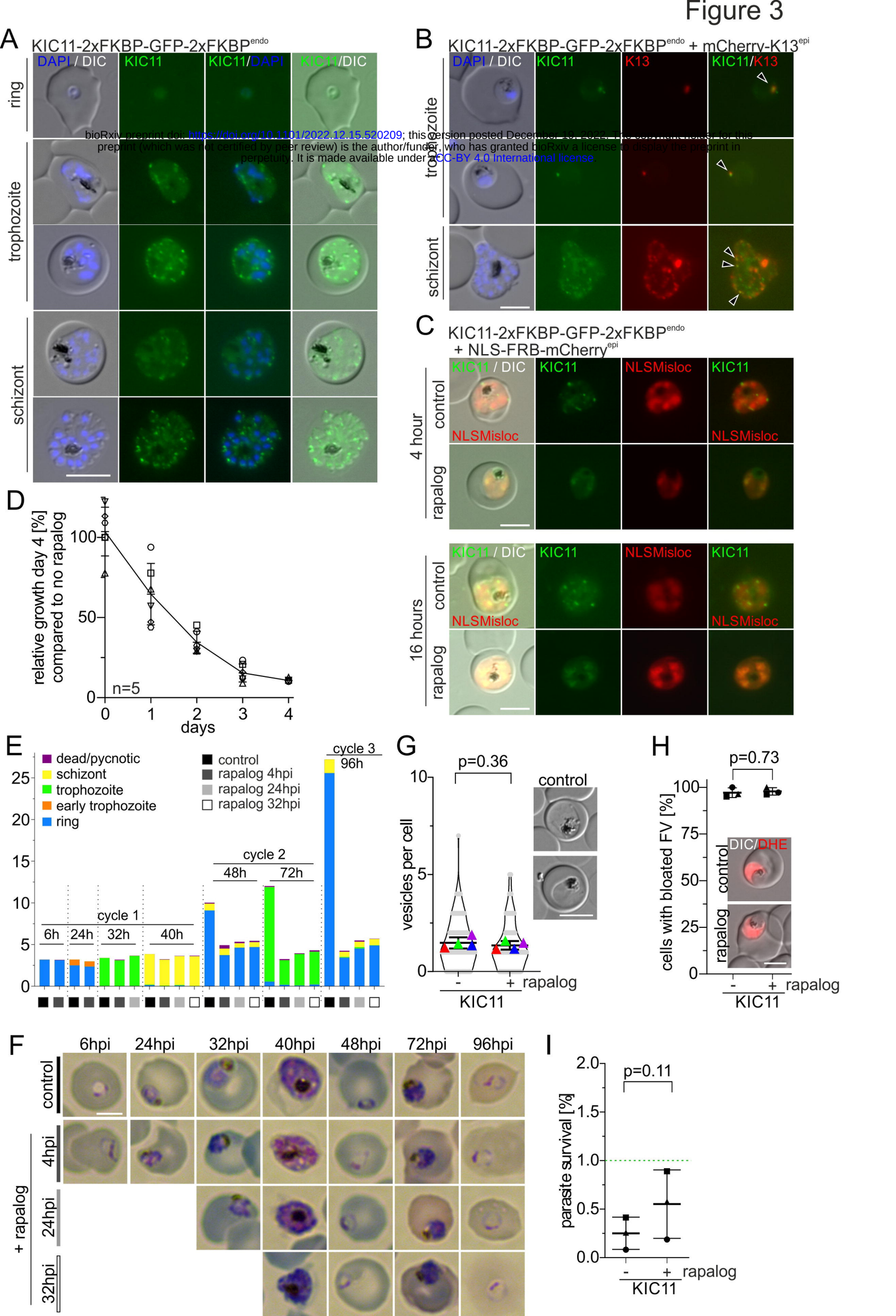

Figure 4

Figure 5

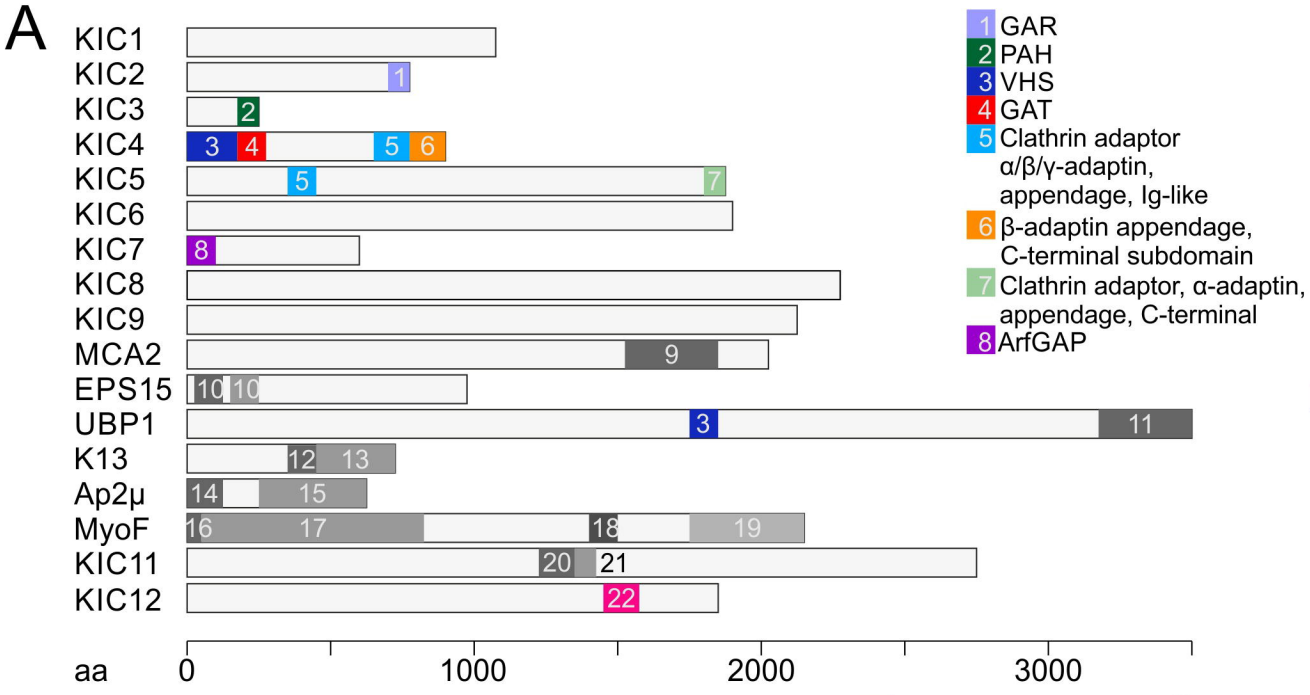

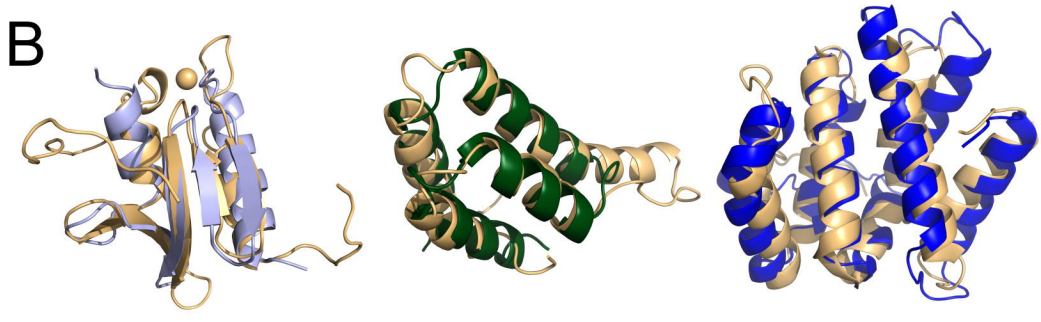

KIC2 701-771 vs.
GAR domain (1V5R)
RMSD 2.8 Å over 72 aa

KIC3 183-249 vs.
PAH domain (1G1E)
RMSD 2.3 Å over 64 aa

KIC4 1-169 vs.
VHS domain (1ELK)
RMSD 3.3 Å over 144 aa

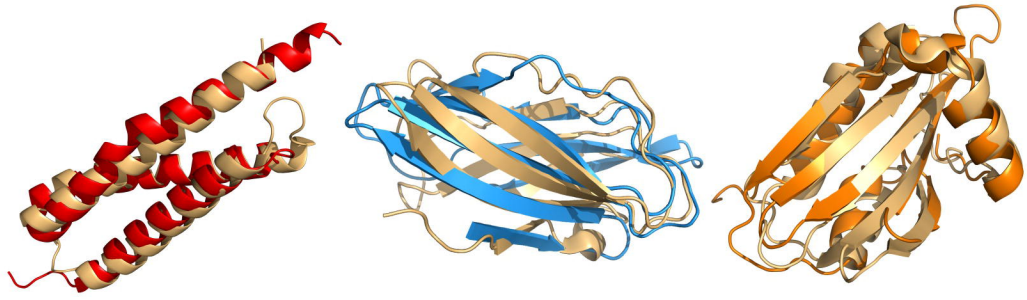

KIC4 170-268 vs.
GAT domain (1WRD)
RMSD 2.5 Å over 88 aa

KIC4 661-764 vs.
clathrin adaptor α/β/γ (2IV9)
RMSD 3.8 Å over 69 aa

KIC4 774-888 vs.
β adaptin app. (2IV9)
RMSD 3.8 Å over 69 aa

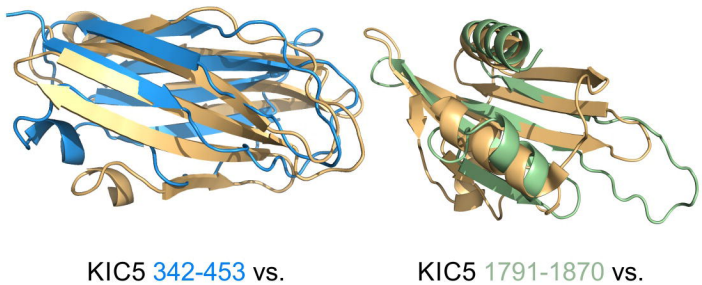

KIC5 342-453 vs.
clathrin adaptor α/β/γ (1KYF)
RMSD 4.0 Å over 8 aa

KIC5 1791-1870 vs.
clathrin adaptor α (1KYF)
RMSD 3.9 Å over 72 aa

KIC7 8-83 vs.
ArfGAP domain (2D9L)
RMSD 3.4 Å over 72 aa

UBP1 1741-1853 vs.
VHS domain (1VDY)
RMSD 3.6 Å over 104 aa

KIC12 1454-1570 vs.
PAP domain (3ZK4)
RMSD 4.9 Å over 112 aa

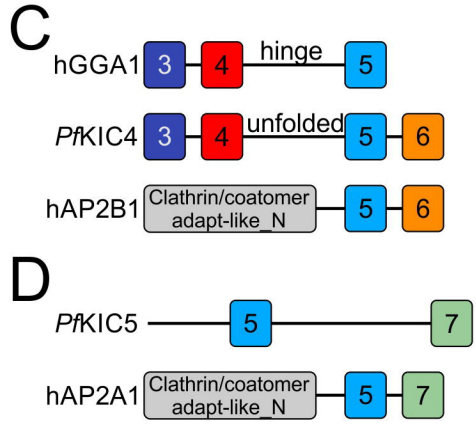

E

K13 compartment proteins

link endocytosis or ART resistance			
yes		no	
Name	VTD	Name	VTD
KIC4	+	KIC1	-
KIC5	+	KIC2	-
KIC7	+	KIC3	-
KIC12	-	KIC6	-
AP2µ	+	KIC8	-
EPS15	+	KIC9	-
MCA2	-	KIC11	-
UBP1	+		
K13	-		
MyoF	-		